High-resolution scanning tunneling microscopy imaging of Si(1 1 1)-7 × 7 structure and intrinsic molecular states

2014 J. Phys.: Condens. Matter 26 394001

(http://iopscience.iop.org/0953-8984/26/39/394001)

IOP Publishing Journal of Physics: Condensed Matter

J. Phys.: Condens. Matter **26** (2014) 394001 (23pp) doi:10.1088/0953-8984/26/39/394001

Topical Review

High-resolution scanning tunneling microscopy imaging of Si(1 1 1)-7×7 structure and intrinsic molecular states

Haiming Guo, Yeliang Wang, Shixuan Du and Hong-jun Gao

Institute of Physics, Chinese Academy of Sciences, PO Box 603, Beijing 100190, People's Republic of China

E-mail: hjgao@iphy.ac.cn

Received 29 March 2014, revised 23 April 2014
Accepted for publication 28 April 2014
Published 12 September 2014

Abstract

We review our achievements in exploring the high resolution imaging of scanning tunneling microscopy (STM) on the surface and adsorbates in a ultra-high vacuum system, by modifying the STM tip or introducing a decoupled layer onto the substrate. With an ultra-sharp tip, the highest resolution of Si(1 1 1)-7×7 reconstruction can be achieved, in which all the rest atoms and adatoms are observed simultaneously with high contrast. Further functionalization of STM tips can realize selective imaging of inherent molecular states. The electronic states of perylene and metal–phthalocyanine molecules are resolved with special decorated tips on metal substrates at low temperature. Moreover, we present two kinds of buffer layer: an organic molecular layer and epitaxially grown graphene to decouple the molecular electronic structure from the influence of the underlying metallic substrate and allow the direct imaging of the intrinsic orbitals of the adsorbed molecules. Theoretical calculations and STM simulations, based on first-principle density function theory, are performed in order to understand and verify the mechanism of high-resolution images. We propose that our results provide impactful routes to pursue the goal of higher resolution, more detailed information and extensive properties for future STM applications.

Keywords: scanning tunneling microscopy, high resolution, functionalized tip, buffer layer, Si(1 1 1)-7×7 surface, molecular orbitals

(Some figures may appear in colour only in the online journal)

1. Introduction

Based on the concept of electron quantum tunneling, Binnig and Rohrer *et al* invented the first scanning tunneling microscope (STM) and observed tunneling through a controlled vacuum gap in 1982 [1]. Over the subsequent thirty years, STM has been proven to be a powerful modern research technique that allows investigation of the morphology and the local electronic states of solid surfaces, or the nanostructures on them, to extremely high spatial and energy resolutions. Moreover, STM also provides an exceptional tool for manipulating, modifying, and spectroscopy of adsorbed atoms and molecules on surfaces [2–5]. Higher spatial and energy resolution, more powerful and extensive functions are always the goal for scientists working in STM fields. The probe's size, shape, and chemical composition at the STM tip apex decisively influences resolution; in general, sharper tips offer higher resolution and performance. A tremendous amount of work has been done to develop ultra-sharp tips and stabilize their fabrication technology [6–8], since a sharp tip is extremely important for high resolution atomic imaging.

Scanning probe microscopy have also been widely applied to investigate the adsorption structures and electronic states of organic functional molecules on solid surfaces over a long decade [9–11]. These researches are of importance with regard

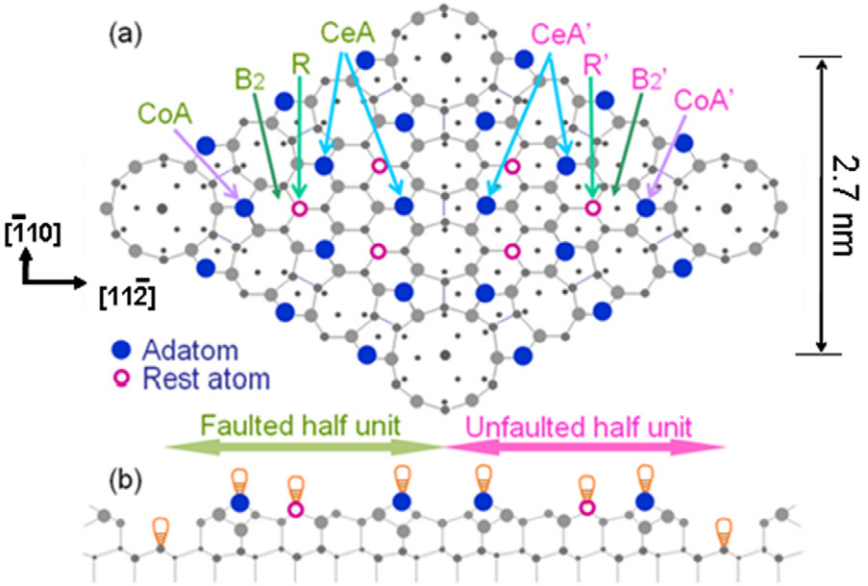

Figure 1. Schematic diagram for Si(1 1 1)-7×7 DAS model. (*a*) Top view: atoms on (1 1 1) layers at decreasing heights indicated by dots of decreasing sizes. (*b*) Side view: dangling bonds locate at the topmost of all adatoms, rest atoms and holes. The sites of corner-adatom, center-adatom, and rest-atom in FHUC (labeled CoA, CeA, and R, respectively), and corresponding sites in UHUC (labeled CoA', CeA' and R', respectively), are identified by arrows. Positions B_2 in FHUC, and B_2' in UHUC are also denoted by arrows.

to both the fundamental aspects of the organic–inorganic interface at the single molecule level, and the potential applications in molecular electronics. In this respect, researchers pursue imaging molecular structures at higher resolutions, allowing direct observation of detailed molecular orbitals and thus providing a deep understanding of the molecule–substrate interaction and reactions at a sub-molecular, or even atomic, scale. This could be accomplished by decoupling molecules from the substrate: for example, by using an ultra-thin insulating film [12, 13], a molecular layer between molecules and metal substrates [14, 15], physisorbed molecules [16–19], or a semiconductor substrate [20]. An alternative way to get high-resolution images of molecules is to functionalize the STM tip by attaching a molecule at its apex [21–25]. It has been proven that adsorbates at the tip apex can change the chemical contrast of the molecular layer on metal surfaces [21–23]. Also, a functionalized tip with CO or C_2H_4 has been found to increase the resolution of STM imaging of small molecules [24, 25]. Reciprocally, the unexpected resolution and symmetry of experimental images could help to extract the realistic chemical composition and orientation of the tip from STM image simulations [26]. Recently, by functionalizing the tip apex with suitable and well-defined terminations and measuring the short-range chemical forces, some exciting developments, based on atomic force microscopy (AFM) techniques, have also been achieved: such as, chemical identification of individual surface atoms [27], resolving single atoms within a molecule [28], and observing the molecular hydrogen bonds [29].

In this paper, we will first review our achievement in exploring the high atomic resolution imaging by STM with an ultra-sharp tip, in which all the rest atoms and adatoms of Si(1 1 1)-7×7 surface can be observed simultaneously with unprecedented high-contrast. In the second part, STM tips are further functionalized to realize selective imaging of molecular states at low-temperature. The molecular states of perylene and metal-phthalocyanine molecules are resolved with special decorated tips. Finally, two different kinds of buffer layers, an organic molecular layer on a metal substrate and epitaxially grown graphene on Ru(0001), are presented. The buffer layers can decouple the molecular electronic structure from the influence of the metallic substrate, thus allowing high resolution STM imaging of the intrinsic electronic orbitals of the adsorbed molecules.

2. Resolving the rest atoms on Si(1 1 1)-7×7 with STM

2.1. The Si(1 1 1)-7×7 structure and STM

The 7×7 reconstruction of Si (1 1 1) is a well-known reconstructed semiconductor surface in surface sciences due to the importance of silicon-based electronics. The surface was imaged in real space for the first time by using STM soon after the birth of this new instrument [30]. Its structure was finally determined in 1985 by Takayanagi *et al* after a detailed analysis of transmission electron diffraction data in a combination with low energy electron diffraction (LEED) results and the real space STM images [31]. The atomic arrangement of the reconstruction surface can be described as the dimer-adatom-stacking fault (DAS) model, as schematically shown in figure 1. This model consists of nine dimmer bonds, 12 adatoms, and a stacking fault between second and third layer atoms in each unit cell. Additional features are corner holes and six unsaturated dangling bonds of six exposed 'rest atoms' in the layer below the adatoms. The 12 adatoms and six rest atoms are evenly distributed in the faulted half unit cell (FHUC) and unfaulted half unit cell (UHUC).

The structures of the Si(1 1 1)-7×7 surface have been extensively investigated with STM [32–37]. STM demonstrations on the atomic topography of a clean Si(1 1 1)-7×7

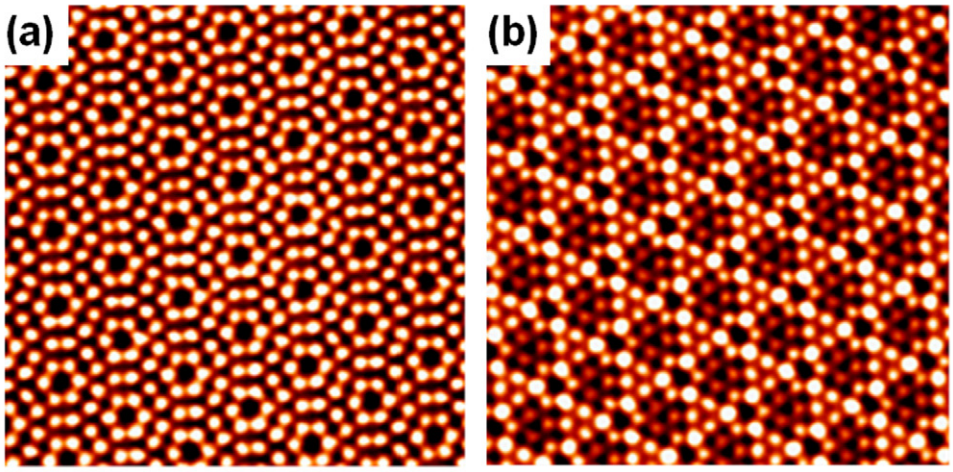

Figure 2. Typical atomic resolution STM images of Si(1 1 1)-7×7 surface. The bright spots mark only the 'dangling bonds' of adatoms. (*a*) Empty states. (*b*) Occupied states. The adatoms on the faulted half are brighter than that on the unfaulted half.

surface commonly show the topmost adatoms, as in figure 2. In the empty state STM image, i.e. with a positive sample bias voltage, the 12 adatoms in one unit cell have the same brightness, while the occupied state image reveals that the adatoms on the faulted half are brighter than that on the unfaulted one. Many *ab initio* caculations for the electronic structure on the 7×7 unit have been carried out. The surface is electronically metallic, with the corner atoms on the faulted half having the highest DOS near the Fermi energy. Furthermore, the states of dangling bonds of the adatoms is about 0.4 eV below E_F, while the states of dangling bonds of rest atoms is about 0.8 eV below E_F [38]. The tunneling current in STM of Si(1 1 1)-7×7 surface originates from these dangling bonds. Voltage-dependent imaging shows that the protrusions depend on the polarity and do not represent the positions of the atoms, but rather the maxima of the LDOS. STM is very sensitive to the states closest to the sample Fermi Energy (E_F), so the mapping of rest atoms with dangling bond states far from E_F is difficult to carry out.

On the mapping of rest atoms on a Si(1 1 1)-7×7 surface, some saddle points at the position expected for the rest atoms were reported by Avouris *et al* [32] and Nishikawa *et al* [33] using STM. Some special techniques were used to obtain the images of the Si(1 1 1)-7×7 surface at atomic scale resolution: Lantz *et al* [34] used scanning force microscopy and Giessibl *et al* [35, 36] used atomic force microscopy. Sugimoto *et al* have successfully identified the three constituent atomic species (Si, Sn, and Pb) on Si(1 1 1) with non-contact dynamic force microscopy by detecting the short-range forces between the outermost atom of the tip's apex and the surface atoms [27]. Sutter *et al* [37] selectively mapped the rest atoms, at the price of suppressing the adatom spots with a monocrystalline semiconductor tip, since the energy gap can suppress tunneling from the adatoms at a certain sample bias. However, the adatoms and the rest atoms of the Si(1 1 1)-7×7 surface are still not clearly distinguished simultaneously in a STM image. This inability has led to the perception that the measured tunneling current for semiconductor materials comes mostly from states near the Fermi level, instead of further away, due to the exponential dependence of the tunneling probability on the energy level position [39].

Here we present our finding that, by using ultrahigh-vacuum (UHV) STM, the resultant images not only clearly show the 12 adatoms but also the six rest atoms per (7×7) unit cell of the Si(1 1 1) surface with high contrast. Careful preparation of the STM tips (reducing the radius of the apex) is the key to success and our first-principles calculations reveal a geometric hindrance effect of the apex for such complex surfaces.

2.2. Simultaneous imaging of the rest atoms and adatoms

The experiments were performed using a ultrahigh-vacuum STM system with a base pressure of ~ 5×10^{-11} mbar. N-doped Si(1 1 1) substrate (ρ ~ 0.03 Ω cm, thickness ~ 0.5 mm) was degassed at about 650 °C in the UHV chamber for several hours, subsequently flashed at 1200 °C for 20 s, rapidly lowering the temperature to about 900 °C, and then slowly decreasing the temperature at a pace of 1–2 °C/s to room temperature. Finally, an atomically flat and clean (7×7) reconstruction was obtained. Sharp STM tips were made of a polycrystalline tungsten wire etched electrochemically in NaOH.

Figure 3(*a*) shows STM images with high contrast between adatoms and rest atoms. They demonstrate simultaneously the adatoms and the rest atoms, that is, 18 topographic maxima per (7×7) unit cell. By zooming in, a high-resolution image with a scanning area of 8 nm × 8 nm presents more clearly all adatoms and rest atoms, as shown in figure 3(*b*). On the UHUC side, the rest atoms appear to have almost the same brightness as the central adatoms, whereas in the FHUC, the rest atoms appear to have considerably less brightness than the central adatoms. The line profile in figure 3(*c*) shows the positions and height differences of the six distinct types of atoms (labeled 1 to 6) along the solid line in figure 3(*b*). The ranking of height of these atoms is: 1 is the highest, then 3 and 6 follow, with 2, 4 and 5 being the lowest. The rest atom (site 2) on the FHUC side is at the same level as the rest atom (site 5) on the UHUC side, and they are both even at the same level as the central adatom (site 4) on the UHUC half side. The high

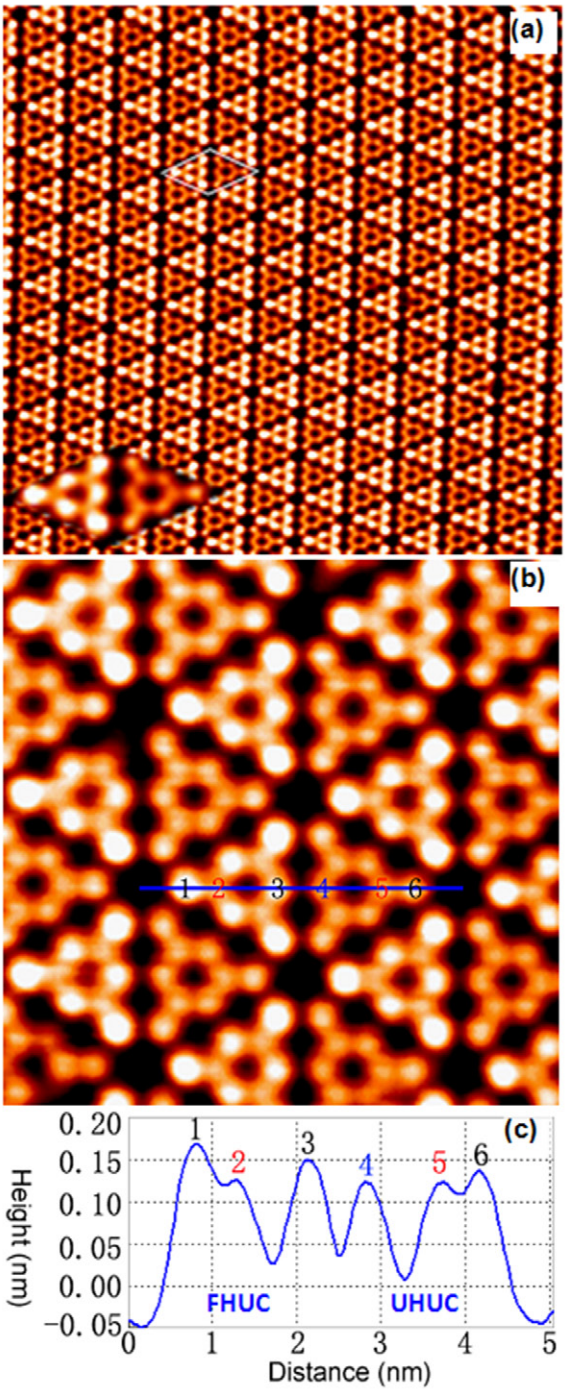

Figure 3. Filled states STM images of Si(1 1 1)-7×7 surface reveal 12 adatoms and 6 rest atoms per unit cell. (*a*) The image extends over an area of 30 nm × 30 nm. The amplified (7×7) unit cell is indicated in the inset, and a (7×7) unit cell is depicted with a rhombus; (*b*) amplified image with scanning area 8 nm × 8 nm. Both images are recorded with sample bias voltage of −1.5 V and tunneling current of 0.3 nA. (*c*) The line profile taken along the line in (*b*), labels '1', '2', '3' denote the corner adatom, rest atom, center adatom in faulted half unit (FHUC) and labels '4', '5', '6' denote the center adatom, rest atom, corner adatom in unfaulted half unit (UHUC), respectively.

contrast between rest atoms and adatoms is even better than the previous results obtained by using scanning force microscopies [34–36]. To our best knowledge, it is the first time that all the rest atoms and adatoms on a Si(1 1 1)-7×7 surface are simultaneously demonstrated with high contrast in an STM topographic image. The emergence of rest atoms will be further rationalized as follows by theoretic simulation.

The defect of a missing corner adatom in figure 3(*b*) has no influence on the adjacent rest atom, and the rest atom is still visible and stays in its normal position without any lateral distortion. So the absence of a local adatom does not affect the geometric structure of its surrounding atoms in a (7×7) unit cell. This result coincides with recent reports about the local structure of adatom vacancies on a Si(1 1 1)-7×7 surface [40]. Chen *et al* conducted STM dI/dV mappings on adatom vacancies and found that the adatom vacancies showed different local electronic structures to the normal adatom but there was no effect on the geometric or electronic structures of the nearby rest atom.

A series of STM images, obtained at different sample bias voltages, illustrate that the emergence of rest atoms is dependent on the sample bias voltage, as shown in figure 4. At lower bias voltages of −0.5 V and −0.6 V, the images (see figures 4(*a* and *b*)) only show 12 adatoms in each (7×7) unit cell. This suggests that the electronic states of the adatoms are closer to the Fermi level than that of the rest atoms. The absence of the rest atoms suggests that the electronic states of the rest atoms are outside the range of the bias when the value of the sample bias is very low. By increasing the bias voltage, the rest atom spots can be visible at the sample bias voltage less than −0.7 V, as shown in figure 4(*c*–*f*). This clearly reveals that the dangling bond states of the rest atoms locate at about 0.7 eV below the Fermi energy (E_F), which is in excellent agreement with experimental results measured by the method of current imaging tunneling spectroscopy (CITS). In 1989, Hamers *et al* measured the electronic band structure of Si(1 1 1)-7×7 surface by using CITS. They provided knowledge of the dangling bond states of adatoms (about 0.35 eV below the E_F) and rest atoms (about 0.8 eV below the E_F [38]).

The STM observations presented here are in sharp contrast to previous STM studies, which in most cases showed images similar to figure 5(*a*) with 12 protrusions in each (7×7) unit, irrespective of the bias voltages (somewhere between −2 V to 2 V). A common explanation [39] for the absence of the rest atom spots in the images relies on the fact that the tunneling probability depends on the thickness of the tunneling barrier. Because the tunneling current is inversely proportional to the exponential of the thickness, the lower electronic state locating in the valence band corresponds to the smaller tunneling current. The rest atoms are invisible but the adatoms are visible because the former have significantly lower energies than the latter. This argument, however, contradicts the theoretical prediction that the dangling bond states of the rest atoms extend into the vacuum region like the adatoms [41]. Also, because the rest atoms are about 4.6 Å away from the nearest adatoms, if one has an infinitely sharp tip positioned right above the rest atom, there is no reason to believe that the adatoms have the effect of screening the rest-atom tunneling. If the tunneling current from the rest atom was indeed weak, one could move the tip closer to the surface in a constant current STM mode. So this common explanation is questionable.

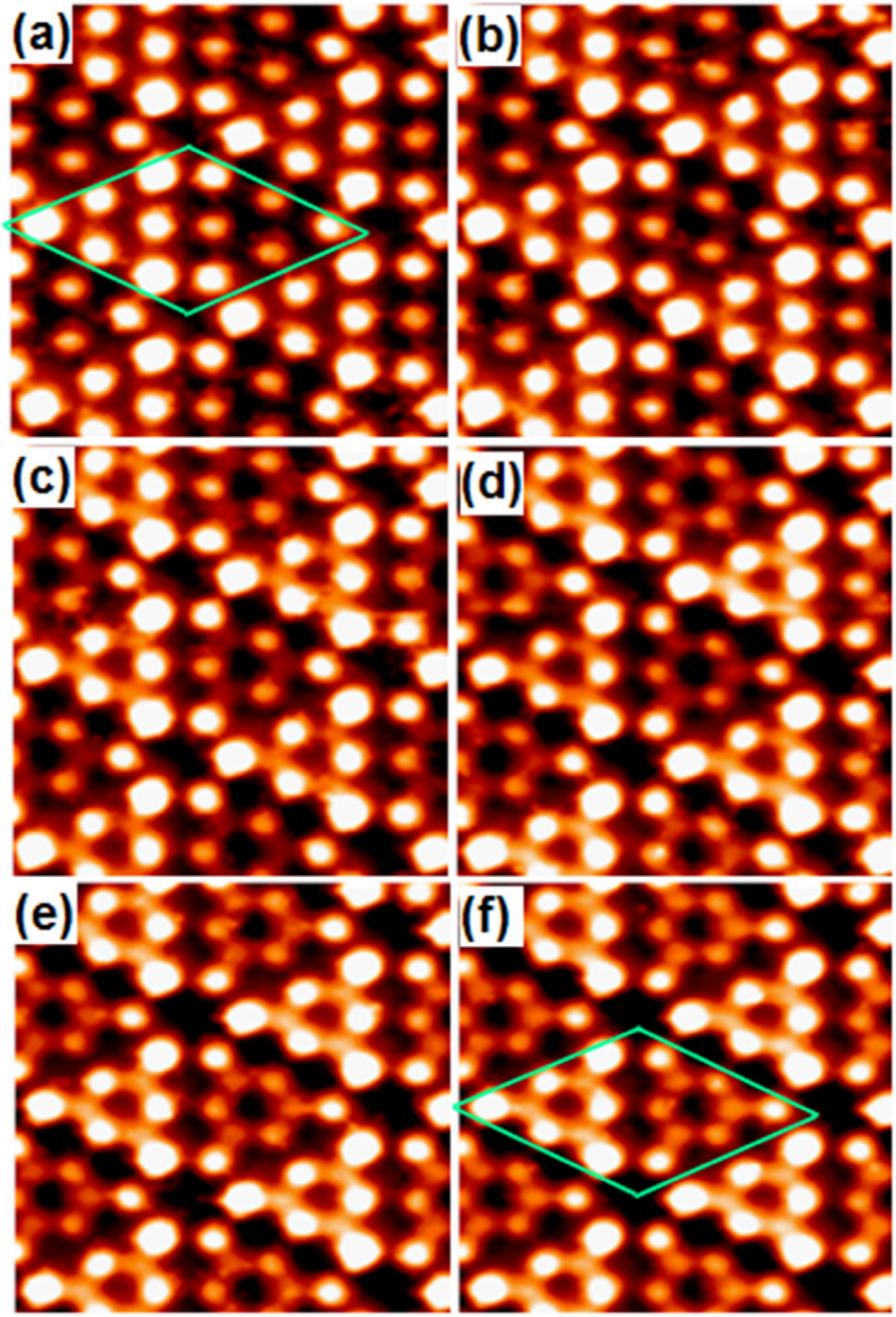

Figure 4. STM images of Si (1 1 1)–7 × 7 surface with different sample bias voltages: (*a*) −0.5 V; (*b*) −0.6 V; (*c*) −0.7 V; (*d*) −0.8 V; (*e*) −0.9 V; (*f*) −1.0 V, respectively. The rest atoms appear at sample voltages less than −0.7 V. All images are taken at $I_t = 0.4$ nA in a scanning area of 5 nm × 5 nm.

Another possible explanation concerns tip contamination: a few silicon atoms might be accidentally picked up by the tungsten tip during the scan, resulting in a semiconductor tip instead of the original metallic tip. Indeed, recently it has been shown that an InAs semiconductor tip [37] could be used to enhance rest-atom visibility by utilizing the second gap above the fundamental gap of InAs material (both lie in the Brillouin zone center) to suppress tunneling current from high-lying adatom states. However, a previous study [42] has also shown that the local electronic structure of a typical metal/semiconductor interface remains metallic until several monolayers into the semiconductor. Thus, it is unlikely, in the present case, that Si atoms are adsorbing, unless the thickness of the contaminant layer exceeds the effective screening length of the Si.

2.3. First-principles calculations and simulations

It is impractical for us to experimentally determine what might have happened to the few tips that worked so remarkably well. Instead, we look for a plausible explanation from theory

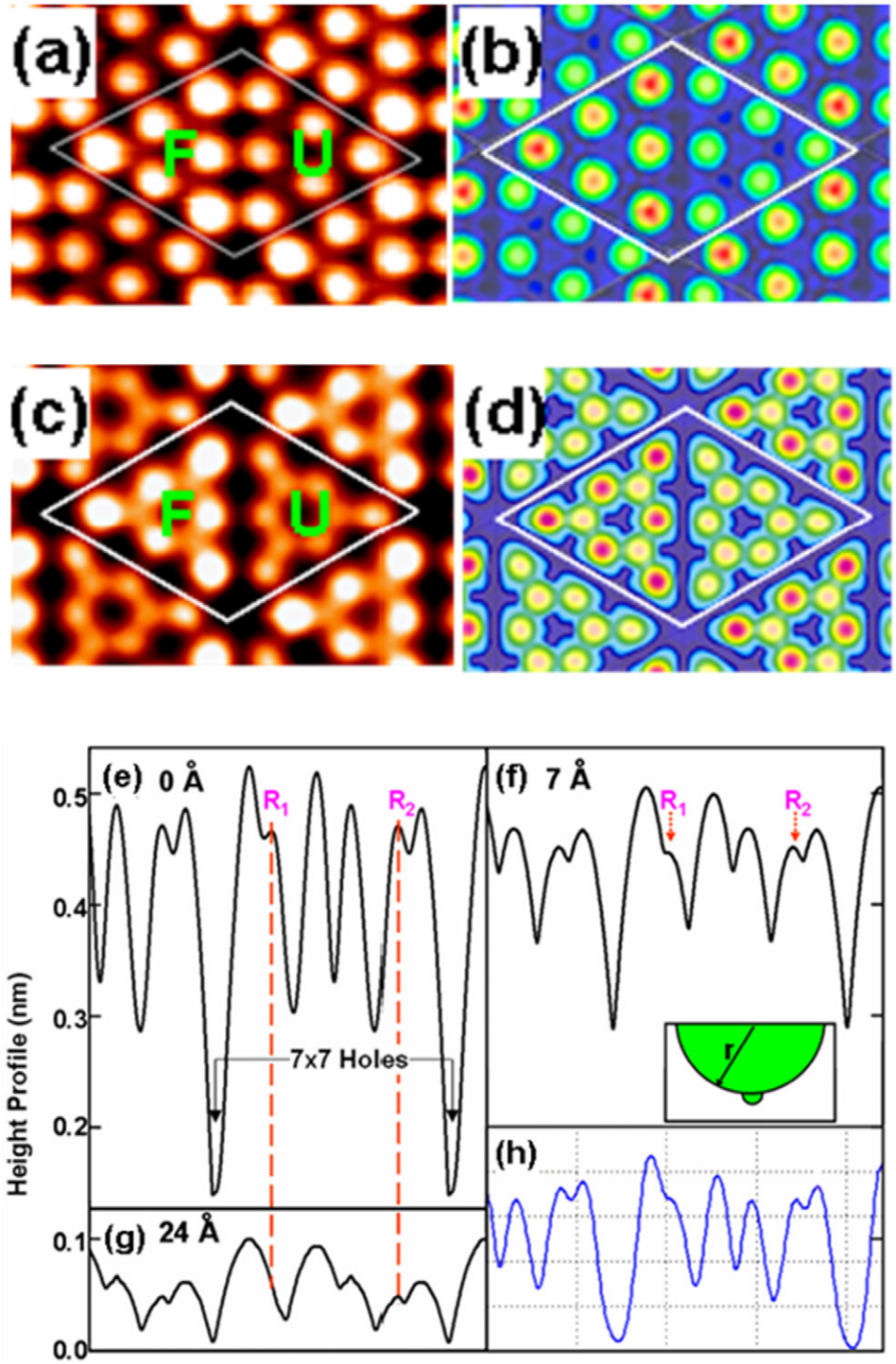

Figure 5. (*a*), (*c*) The experimental STM images with bias voltage of −0.57 and −1.5 V, and tunneling currents of 0.3 and 0.41 nA, respectively. F and U depict the FHUC and UHUC, respectively. (*b*), (*d*) Calculated STM images for Si(1 1 1)–7 × 7 with bias voltages of −0.57 and −1.5 V, respectively. The red peaks are about 2 Å above the dark blue borderlines. (*e*), (*f*) and (*g*) are the calculated height profiles along the diagonal of the (7 × 7) unit cell with tip apex radius $r = 0.0$, 7.0, and 24.0 Å, respectively. (*h*) The experimental profile. Inset schematically shows an STM tip with an adsorbed cluster beneath the apex.

calculations. Our collaborators carried out the calculation by using first-principles DFT, as implemented in the VASP codes [43]. The Vanderbilt ultrasoft pseudopotential [44] was used with a cutoff energy equal to 170 eV and one special k-point in the Brillouin zone sum. The surface unit cell contains a slab of six Si layers (without counting the Si adatoms) and a vacuum layer equivalent to six Si layers. The front surface contains the (7 × 7) reconstruction in the Takayanagi model, whereas the back surface is passivated by hydrogen. Except for the very bottom layer, all the Si atoms are fully relaxed to minimize the system's total energy.

Apparently, the actual tip morphology is also complex, possibly with additional atoms adsorbed at the end of the apex, as shown in the inset in figure 5(*f*). Because only the

lower semispherical part of the tip can be in close proximity with the surface, here the tip is replaced by a sphere of radius *r*. To further simplify the calculations, only the line-scans along the diagonal of the (7×7) unit cell are considered in our simulations.

Figure 5(*a*) shows the STM image of the Si(1 1 1)-7×7 surface at a sample bias of −0.57 V. The appearance shows a significant contrast between the FHUC and UHUC of the (7×7) unit. At this low sample bias, the electronic states of the rest atoms are outside the range of the bias. Thus, the STM topography here reveals only the 12 topmost adatoms. The adatoms in the FHUC appear noticeably brighter than those in the UHUC. In each half, the adatoms at the corners appear also slightly brighter than those near the center. These qualitative features are in good agreement with the calculated real-space charge distribution at this particular bias [figure 5(*b*)]. Figure 5(*c*) shows the STM image at a sample bias −1.5 V. Images of similar quality can be repeatedly reproduced over a large area up to 30 nm × 30 nm [figure 3(*a*)]. We can clearly see both the adatoms and the rest atoms. On the UHUC, the rest atoms appear to have almost the same brightness as the central adatoms, whereas on the FUHC, the rest atoms appear to have considerably less brightness than the central adatoms. These observations are again in excellent agreement with the calculated real-space charge distribution at the experimental bias in figure 5(*d*).

Figure 5(*e*) shows the calculated line-scan at −1.5 V with an infinitely sharp tip, i.e., r = 0, as has been done before in most STM image simulations [45]. A sharp tip is also assumed in calculating the images in figure 5(*b*) and (*d*). Now, we trace this r = 0 curve with a disk of radius r, which is a two-dimensional representation of the three-dimensional sphere, to explore geometric hindrance. It is assumed that at each tip position, tunneling takes place at only one spot on the disk. This is reasonable in most cases because tunneling probability diminishes exponentially with distance. However, there are a few exceptions where the disk is nearly or equally distanced from the r = 0 curve, i.e., at or near the local symmetry points. For simplicity, however, such a tunneling-current doubled effect is ignored in our simulation.

Our results show that, for a small disk radius mimicking adsorbed clusters, the line-scan is essentially the same as in figure 5(*e*). Figure 5(*f*) shows the simulated result for r = 7 Å. At this radius, while none of the main surface topological features have been lost, the overall shape of the line-scan has been significantly modified, noticeably the depth of the profile, and the size of the atoms is noticeably larger than those in figure 5(*e*). Figure 5(*g*) shows the simulated result for *r* = 24 Å. At this radius, the rest atom on the FHUC has completely vanished. Even for the UHUC, the contrast between the much more visible rest atom spots and the adatom spots has been greatly reduced. Thus, it is clear that the attainable size of the tip apex is the crucial factor in imaging the true charge distribution on the (7×7) surfaces. Figure 5(*h*) shows the corresponding line-scan determined by our experiment. Despite the simplicity of the model, the calculated result for *r* = 7 Å in figure 5(*f*) is in quantitative agreement with experimental observation.

It is now understood that STM probes the real-space charge distribution near the E_F in a rather delicate way that may or may not reveal the unperturbed real-space charge distribution of the surfaces. Here we show the calculated and experimental voltage-dependent charge distributions of the Si(1 1 1)-7×7 surface, which reveals simultaneously both the 12 adatoms and the six rest atoms in each (7×7) unit cell [46]. The emergence of the rest atom is dependent on the bias voltage and rest atom spots can be visible at a sample bias voltage of less than - 0.7 V. First-principle electronic structure calculations also show a strong dependence of the charge distribution on the bias voltage: 12 spots at−0.57 V for the 12 adatoms [see figure 5(*b*)], whereas 18 spots at −1.5 V for the 12 adatoms plus six rest atoms [see figure 5(*d*)]. Our results suggest that a geometric hindrance, due to the finite size of the tip apex, could be the reason. This finding should invoke significant research interest in the design and fabrication of the STM tip and its application in exploring more detailed information about surface reconstructions and nanostructures of the physical properties of nanosystems.

3. Investigation of molecular states with functionalized STM tips

The above work demonstrates high resolution imaging of STM on a semiconductor Si(1 1 1) surface with a very restricted tip apex. The continuous refinement of analyzing techniques in STM has made it possible to analyze even the atomic-scale electronic properties of adsorbate-substrate systems. A number of investigations have recently focused on selective measurements of individual molecular states or metal states [47, 48]. These experiments are of great interest for molecular electronics and nanoscale device fabrication [12, 49–51]. However, selectively imaging molecular or metal states in STM measurements is usually prevented by the complex coupling of electronic states of metal surfaces, organic adsorbates, and metal tips. A selective analysis of molecular states on metal surfaces was usually achieved only in a few cases by tuning the bias range of the STM. In electrochemistry measurements [52, 53], functionalizing metal electrodes with organic polymers can exhibit high selectivity. This method can be extended to fabricate functional STM tips, which are sensitive to molecular or substrate electronic states. Boehringer *et al* obtained a atomically resolved Ag(1 1 0) substrate lattice, with an amplified corrugation, when an anthracene molecule was dragged onto the tip apex, which is weakly bound ontp the metal substrate. It suggests that the STM images can reflect an interplay between tip molecule and molecule–substrate interactions, and suitable molecules on the surface may be used as sensors to probe the local substrate–adsorbate interaction strength [17].

In this section, we will present our two works on selective imaging of molecular states with functionalized tips by low-temperature STM analysis combined with density functional theory (DFT) calculations and STM image simulations. First, we demonstrate that molecular π states of perylene adsorbed on Ag(1 1 0) can be directly imaged by a clean tungsten tip. By

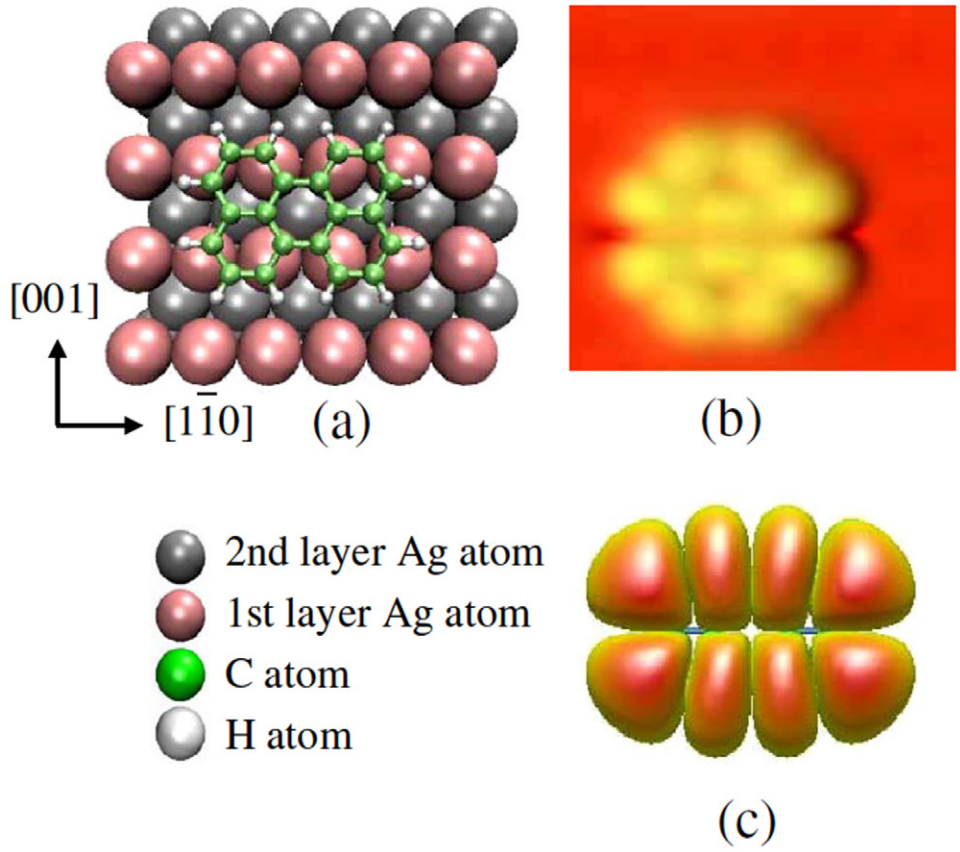

Figure 6. (*a*) Ground state adsorption configuration of perylene molecule on the Ag (1 1 0) surface. (*b*) Charge density of perylene molecule deposited on the Ag (1 1 0) surface. (*c*) Charge density of an isolated perylene molecule in vacuum (from –0.7 to + 0.7 eV relative to the Fermi level).

contrast, functionalizing the STM tip with a perylene molecule leads to a mismatch between the energy levels of the tip and the molecule adsorbates and, instead, images only the metal states of the underlying silver surface. Secondly, by using a special O_2 decorated tip, STM images of metal-Pc molecules on Au(1 1 1) reveal rich intramolecular features caused by the interaction with the highly directional orbitals of the adsorbed O_2 molecules. These results open a new route to discriminate between electronic states of organic adsorbates and states of the metal surface, and have potential applications in fundamental research based on high-resolution electronic states of molecules on metals, concerning, for example, chemical reactions, and catalysis mechanisms.

3.1. Selective analysis of perylene molecular states by functionalized tips

Our experiments are performed in a combined UHV molecular-beam-epitaxy and low-temperature STM system. The base pressure in the experiments is below 3×10^{-10} mbar. An Ag(1 1 0) surface is cleaned by repeated cycles of Ar^+ sputtering (1 keV, 20 min) and subsequent annealing at 700 K (20 min). The bare silver surface is imaged before dosing to confirm its cleanliness. Perylene is thermally evaporated at 395 K onto the Ag(1 1 0) surface. Previous low energy electron diffraction (LEED) experiments show that on an Ag(1 1 0) surface the local adsorption configuration of the perylene molecule does not depend much on the coverage [54, 55]. The coverage of one molecular monolayer (ML) corresponds to about 5.0×10^{13} molecules per cm^2. To isolate the interaction between molecules and the surface from intramolecular interactions, we chose the coverage of 0.6 ML to search for the most optimized adsorption configuration. The normal STM tips were electrochemically-etched poly–crystalline tungsten tips. All given voltages were applied to the sample. All STM images were recorded in a constant current mode at 5 K.

Ab initio DFT calculations are carried out with the Vienna *Ab Initio* Simulation Package (VASP [56]). The Ag(1 1 0) supercells are modeled by a four-layer Ag film with perylene molecules adsorbed on only one side of the surface. This geometry is justified in view of the very low adsorption energies and, consequently, low hybridization of electronic states, which does not give rise to surface dipoles. A vacuum of 17 Å is used to separate the mirror images in the z direction. The ion-electron interactions are described by ultrasoft pseudopotentials. The exchange-correlation potentials are calculated with a generalized gradient approximation, in accordance with Perdew, Burke, and Wang [57]. The energy cutoff for plane waves is 400 eV. The number of k points is varied until the adsorption energies of perylene converge. The same method is also used to calculate the electronic properties of STM tips. All STM simulations presented here are performed with a scattering method developed to the first order in Green's functions [58].

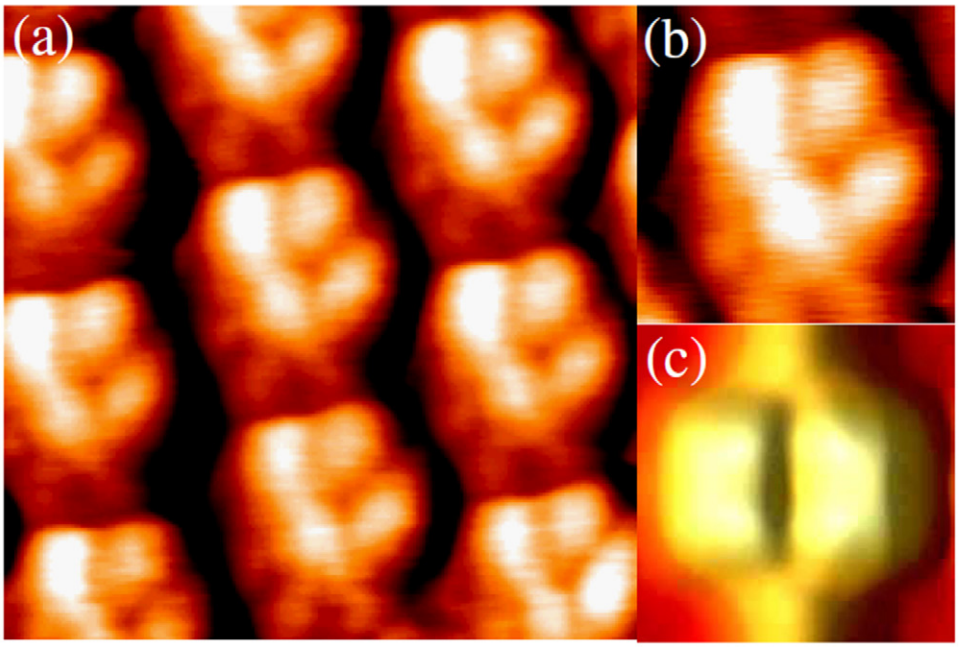

Figure 7. A monolayer of perylene molecules adsorbed on Ag (1 1 0) surface. (*a*) A high-resolution STM image, 3 nm × 3 nm. (*b*) An enlarged image of one perylene molecule of the perylene monolayer in (a), 1.2 nm × 1.2 nm. (*c*) Simulated STM image with a clean tungsten tip. Parameters: $U = +1.8$ V, $I = 90$ pA.

In total, 20 possible structures, varying in orientation and adsorption sites, have been analyzed. We find that the geometry of the molecule leads to an energy penalty of about 0.3 eV, if the central benzene ring is adsorbed on top of the silver rows, and that the molecule is preferably adsorbed with its longitudinal axis parallel to these rows. The physical reason for this behavior is the overlap between the π states of the molecule and the electronic states of the surface. In the ground state adsorption geometry, this overlap is maximized, leading to the maximum binding energy.

Here we present only the most stable configuration. As shown in figure 6(*a*), the center of the perylene molecule is positioned above an fcc hollow site of the Ag(1 1 0) surface. The molecule adopts an orientation in which its long axis aligns parallel to the $[1\bar{1}0]$ direction of the Ag(1 1 0) surface. The adsorption energy per molecule in our calculation is −0.53 eV, which is consistent with thermal-desorption experiments [54]. The weak adsorbate-surface interaction is due to the mismatch of molecular energy levels near the Fermi energy and energy levels of the Ag substrate [20]. Comparing the partial charge density of a perylene adsorbate on the Ag(1 1 0) surface [see figure 6(*b*)] and an isolated perylene molecule in the vacuum [see figure 6(*c*)], it can be seen that the molecular states of perylene remain virtually unchanged rather than hybridize with the electronic states of the Ag surface.

Figure 7(*a*) shows a high-resolution STM image of a perylene monolayer on the Ag(1 1 0) surface. Each perylene molecule is imaged as four bright lobes with an apparent height of 1.5 Å. The twist of the molecule in the experimental STM image is probably due to the lateral intermolecular interactions of perylene adsorbates [59]. Figure 7(*c*) shows a STM simulation image obtained with a clean tungsten tip, which is roughly equivalent to the local charge density (see figure 7(*b*)), i.e., the states, of perylene molecules on a Ag(1 1 0) surface.

At dilute coverage, there is no long-range ordered structure of perylene adsorbates observed by LEED on the Ag(1 1 0) surface [54]. Since the disordered perylene molecules are now far from each other, a tungsten tip can easily be functionalized by picking up a single perylene molecule from the silver substrate. Since tungsten is less noble than silver, the adsorption energy of perylene on tungsten is substantially higher. The actual adsorption energy of perylene on a tungsten tip will be less than −8 eV, calculated from the adsorption on a flat tungsten (1 0 0) surface, due to tip asperities. If only one benzene ring adsorbs to the tip apex, the adsorption energy will be in the range of −1 eV [60] or double the value for the adsorption on Ag(1 1 0). Therefore, the tip can be functionalized by scanning the surface at low coverage with a clean tungsten tip and at sufficiently high currents. At the beginning of the STM scanning, the molecules are imaged as protrusions on the surface. After we modify the tip by applying voltage pulses from the STM tip, the STM images change to a different mode. Thus, we conclude that the ensuing STM images are obtained with a different tip. The only option in this case is a tip functionalized by a perylene molecule. The similar contrast reversal resulted from the molecular adsorption on the tip apex has also been reported for the PTCDA molecules on Ag(1 1 0 [23]).

Changing the bias voltage and current, this functionalized tip can be used to discriminate the energy levels of perylene adsorbates. At the bias voltage of −0.8 V (current 27.5 pA), part of the Ag surface now appears as a protrusion, and the perylene molecules seem to be embedded in the substrate, as shown in figure 8(*a*) and (*d*). Figure 8(*g*) gives our STM simulation with a functionalized tungsten tip. Varying the

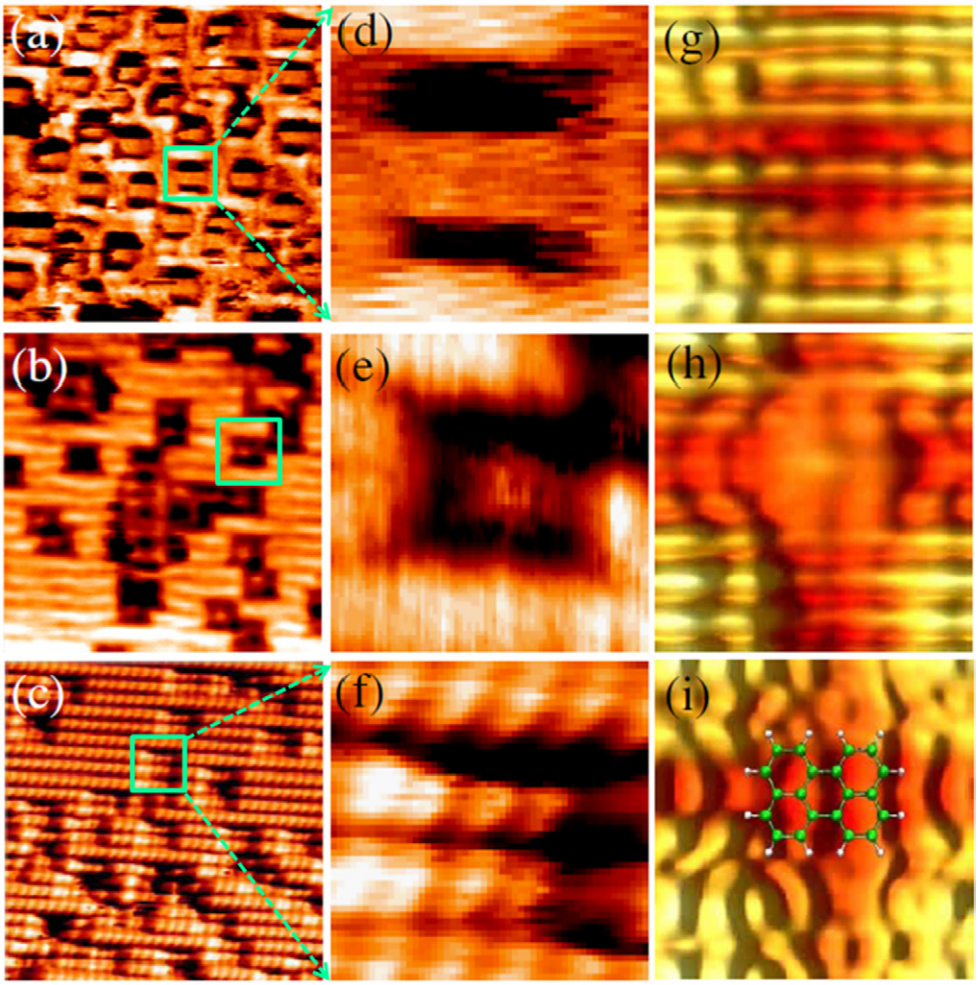

Figure 8. (*a*)–(*c*) STM images of perylene molecules adsorbed on Ag (1 1 0). The green square indicates a single perylene molecule. (*d*)–(*f*) High-resolution details of a single feature in (*a*)–(*c*). (*g*)–(*i*) STM simulations of (*d*)–(*f*) with a tungsten tip functionalized by perylene. The position of the perylene molecule on the surface is indicated (i). Parameters: (*a*) 10 nm × 10 nm, 0.5 ML, $U = -0.8$ V, I = 27.5 pA; (*b*) 7.9 nm × 7.9 nm, 0.6 ML, $U = -0.67$ V, I = 161.5 pA; (*c*) 10 nm × 10 nm, 0.3 ML, $U = -1.5$ V, I = 149 pA.

bias voltage to −0.67 V and changing the current to 161.5 pA [see figure 8(*b*)], the whole Ag surface appears, and the image of the Ag rows in the $[1\bar{1}0]$ direction is obtained. If the bias voltage is further increased to −1.5 V, a current of 149 pA yields a high resolution of the Ag surface while the perylene adsorbates are seen as depressions [see figure 8(*c*)]. Simulations under identical tunneling conditions are shown in figure 8(*h*) and (*i*). All features are reproduced by STM simulations with a perylene-modified tungsten tip.

It's noteable that the central part of the molecule is still visible in figure 8(*h*) and has vanished in figure 8(*i*). The reason for this behavior is the onset of the *d* band on the silver surface, which reaches its maximum density of states around −1.5 eV. At a bias value of −1.5 eV, the protrusion in the middle of the molecule disappears, and the STM images reveal only the atomic positions of the silver surface. The images clearly demonstrate the induced functionality of the tip due to the adsorbed molecule. While the states of the molecule at the surface become invisible due to the increased energy difference to the states of the tip, the continuous *d* band of Ag(1 1 0) gradually provides the majority of tunneling electrons. Correspondingly, we also note that varying the adsorption geometry of perylene on the tungsten tip, e.g. by rotating the molecule with respect to the vertical axis or changing the adsorption site, does not affect the results of the STM simulations. This indicates that most of the tunneling current is transported from the attached perylene molecule, while the influence of the tungsten tip configuration is rather small.

To understand the nature of this intriguing effect, we performed a partial charge density calculation for a perylene molecule on a W(100) film [see figure 9(*a*)]. As shown in figure 9(*b*), the π orbitals of the perylene molecule merge completely with the charge density of the metal surface, which therefore greatly changes the charge density of the clean tungsten tip. The functionality of this tip, i.e., the discrimination of perylene states, is therefore due to the mismatch of energy levels of perylene molecules on the Ag surface and on the modified STM tip.

3.2. Molecular orbitals observation of metal-phthalocyanine with O_2 functionalized tip

The experiments were performed with the same UHV-LT-STM system. The bare Au(1 1 1) surface was prepared by several cycles of Ar^+ ion sputtering and annealing to 700 K,

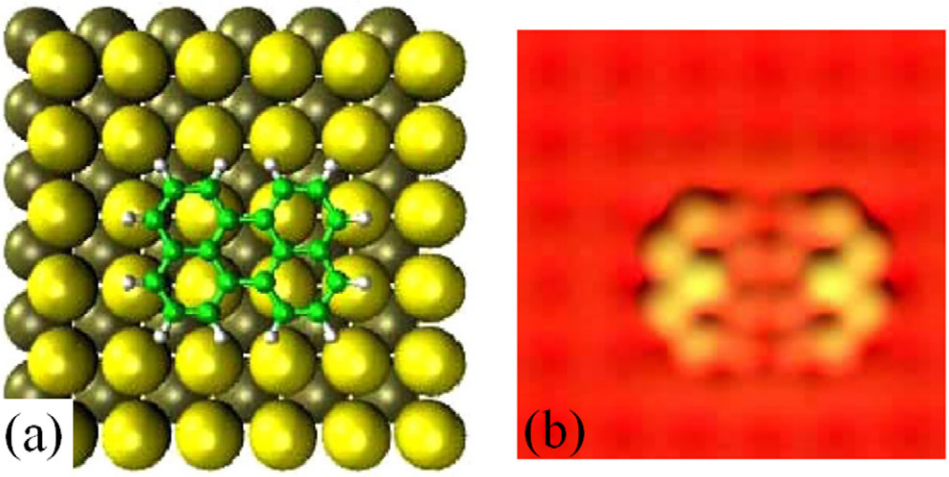

Figure 9. (*a*) Perylene molecule attached to a W(1 0 0) surface. (*b*) Partial charge density of the perylene modified W(1 0 0) surface (from −0.7 to + 0.7 eV relative to the Fermi level).

until a clean surface was confirmed by STM imaging. FePc and ZnPc (Aldrich, 98+%) were thermally evaporated at 540 K with a MBD-LEED technique onto an Au(1 1 1) surface held at 370 K [61, 62]. All STM images were recorded in a constant current mode at 5 K.

Figures 10(*a*) and 11(*a*) show typical STM images of the highly ordered FePc and ZnPc monolayer on Au(1 1 1) obtained by a normal STM tip, respectively. The molecules prefer a commensurate superstructure with a quadratic unit cell. Each molecule has a flat-lying adsorption configuration on the terraces. The FePc molecule is recognized as a four-lobed 'cross' structure with a central round protrusion, while the ZnPc molecule has a four-lobed 'cross' pattern with a central round hole. Both FePc and ZnPc show identical orientations, with the 'cross' directed in the $[1\bar{1}0]$ and $[11\bar{2}]$ directions of the Au(1 1 1) surface. FePc and ZnPc molecules are typical planar D_{4h} symmetric MPc molecules, composed of a flat Pc skeleton with an iron or zinc ion in the central cavity (see the insets of figure 10(*b*) and figure 11(*b*)). The enhanced brightness at the center of FePc is ascribed to a large tunneling current that results from orbital-mediated tunneling through the half-filled d_{z^2} orbital of the Fe ion. In the case of ZnPc, the *d* orbitals of Zn are fully filled and there is no electronic state contributing to tunneling near the Fermi level [63–65]. Therefore the zinc ion of the ZnPc molecule appears as a hole in the STM images. Due to the three-fold symmetry of the Au(1 1 1) surface, the symmetry of the adsorbed planar MPc molecules is reduced from D_{4h} to C_{2v}.

Due to oxygen reduction by metal phthalocyanine (MPc), some oxygen molecules will adsorb within the MPc powder by their strong oxygen-MPc interactions [66–69]. So, a tiny amount of oxygen molecules co-adsorb with the MPc molecules on the Au(1 1 1) surface during the deposition process. In the STM measurements, we purposely approach the STM tip to the MPc monolayer by either increasing the current or decreasing the bias, so that the tip is more likely (compared with normal scanning conditions) to pick up an oxygen molecule. Then we have a small but workable chance to get an O_2 functionalized STM tip. When introducing a tiny number of extra oxygen molecules into the chamber, we do have a higher chance to get a same functionalized tip, directly confirming the O_2-functionalized STM tip experimentally.

Figures 10(*b*) and 11(*b*) present STM images of FePc and ZnPc molecules, respectively, with the high resolution if this functionalized tip is used. Many intramolecular features are revealed in the close-up STM images, as presented in figures 10(*d*) and 11(*d*), respectively. The images obtained with a normal tip (figures 10(*c*) and 11(*c*)) are shown for comparison. The difference in the images of the FePc molecule is most pronounced for the central protrusion. This protrusion appears as a featureless round bump in images with the normal tip, while it appears as a nearly equilateral triangle with the functionalized tip. The specific features are also observed within the molecular lobes. Without considering intensity asymmetry of different lobes, the features within the two lobes of FePc along the $[01\bar{1}]$ direction are mirrored with the $[\bar{2}11]$ direction, while those within the two lobes along the $[\bar{2}11]$ direction are also mirrored with the $[01\bar{1}]$ direction. But the features of lobes in different directions are different, similar to the highest occupied molecular orbital (HOMO) of a free FePc molecule, as shown in figure 12(*a*). It is apparent that the triangular protrusion at the iron position is different from the HOMO of a free FePc molecule, demonstrating a strong effect of the substrate on the center iron. So we can conclude that the interaction between central iron and the substrate should be the main contribution for the whole FePc molecule-substrate interaction. And this triangular protrusion must be induced by the mismatch of symmetry of the FePc molecule and the Au(1 1 1) substrate.

As for ZnPc molecules, the corresponding image retains the round central depression with the functionalized tip, even though the rest of the molecule is substantially better resolved than that with a normal tip. Each of its four lobes shows similar intramolecular features, in which each lobe is divided into four small protrusions with different intensity. This is also similar to the HOMO of an isolated ZnPc molecule (Figure 12(*b*)).

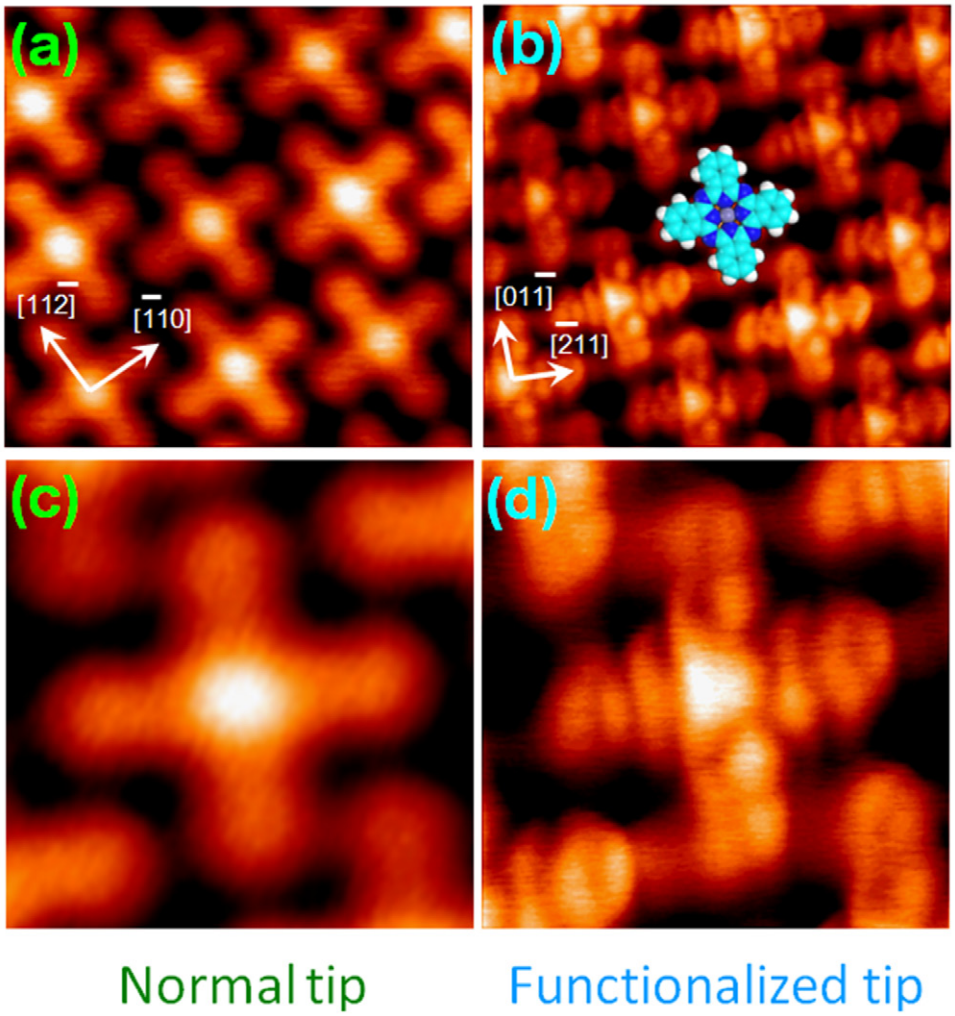

Figure 10. STM topography images of FePc monolayer on Au(1 1 1) surface. (*a*) and (*c*) are obtained with a bare metallic STM tip. (*b*) and (*d*) are obtained with a functionalized STM tip. (*a*) and (*b*) 5 nm × 5 nm, structure of FePc as inset; (*c*) and (*d*) 2 nm × 2 nm. All the images are obtained with $U = -0.4$ V, $I = 0.05$ nA.

Unlike the FePc/Au(1 1 1) system, in which the adsorption changes the center protrusion from round to triangular, the center of ZnPc is still a round hole after adsorption. As the chemical structures of FePc and ZnPc are so similar, this difference must be attributed to their different molecule-substrate interactions resulting from their different central metal ions; that is to say, the interaction between Fe^{2+} and the substrate is stronger than that of the Zn^{2+}-substrate.

In order to fully understand the physical information behind these high-resolution STM images, we performed *ab initio* calculations both for free molecules and molecules on the Au(1 1 1) substrate. For free molecule calculations we used Gaussian 98 at B3lyp/6–31 g* level. For molecules on Au(1 1 1), theoretical calculations were based on DFT, the Perdew-Wang exchange-correlation functional with generalized-gradient corrections [70], projector augmented waves (PAW [71]), and plane waves, as implemented in the VASP code [56]. Due to the huge size of the unit cells we limited the calculations to only one k-point. The energy cutoff in the simulation was 400 eV, the structures were relaxed until the net force on every atom was smaller than 0.02 eV/Å. STM images were calculated with the GREEN code [72, 73], a program based on the extended Hückel theory (EHT [74]). In this program, the tunneling current is calculated explicitly by applying the Landauer formula in which the transmission coefficient was evaluated through a Green's function approach. This allows the precise tip apex geometry and composition to be taken into account, which is essential in the present context.

STM images were simulated using previously DFT optimized FePc (ZnPc) monolayers on Au(1 1 1), with a standard W(1 1 1) tip [75] (single atom terminated pyramid, figure 12(*c*)) and an O_2 molecule attached blunt tip (after removing the end W atom, figure 12(*d*)), respectively. It is commonly assumed that no sub-molecular resolution is achievable with standard STM tips concerning single molecules or a monolayer of adsorbed molecules on a metallic substrate. The difference can be due to the well-known alignment of molecular orbitals with the substrate Fermi level upon adsorption or the fact that the molecular states are merged with the surface electrons to produce a convoluted STM image [14]. The alignment corresponds to a shift of molecular orbitals like the HOMOs and LUMOs. The consequence is that these levels are out of

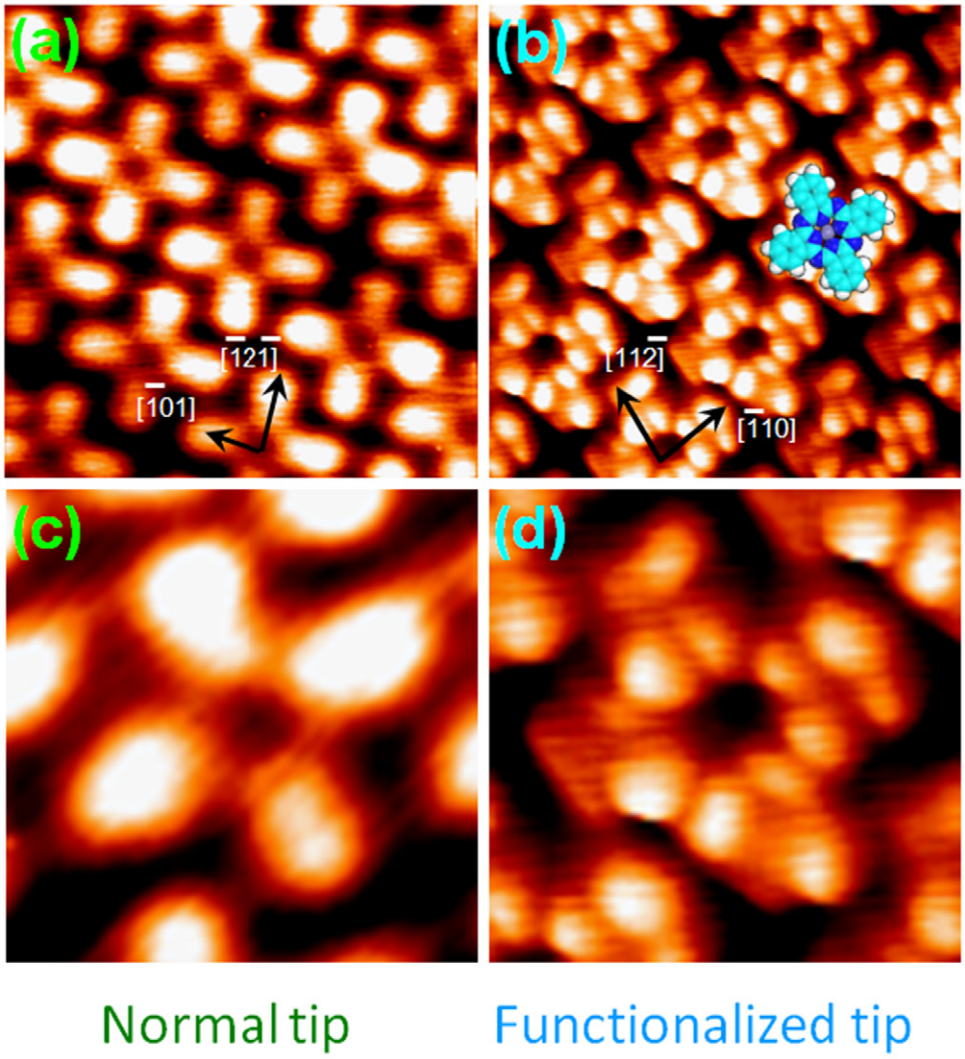

Figure 11. STM topography images of ZnPc monolayer on Au(1 1 1) surface. (*a*) and (*c*) are obtained with a bare metallic STM tip. (*b*) and (*d*) are obtained with a functionalized STM tip. (*a*) and (*b*) 5 nm × 5 nm, structure of ZnPc as inset; (*c*) and (*d*) 2 nm × 2 nm. All the images are obtained with $U = -1.6$ V, $I = 0.05$ nA.

range under standard bias (for example, 0.4 V and 1.6 V for imaging FePc and ZnPc, respectively) with a pure metallic STM tip. With this functionalized tip, however, the adsorption of molecules or impurities creates new localized electronic states that restore the bias range for a sub-molecular resolution. In figure 13(*a*) and (*b*), the calculated projected density of states (PDOS) of the FePc molecule on Au(1 1 1) substrate was presented with the PDOS of the clean tungsten tip and with the PDOS of the O_2 functionalized tungsten tip, with respect to the bias condition used in simulation. It is clear that the oxygen atoms create a new localized electronic state near the Fermi level, which makes the intramolecular features of HOMO of FePc molecule visible.

Our simulation using the pyramidal W-fcc (1 1 1) oriented tip shows a four-lobed 'cross' structure with a round protrusion in the center for FePc/Au(1 1 1) (figure 13(*c*)). The simulation with the same tip also show a 'cross' structure with a round 'hole' in the center for ZnPc/Au(1 1 1) (figure 13(*e*)). Both simulations are in good agreement with the experimental results (figure 10(*c*) and 11(*c*)). The simulations using a blunt tip with one O_2 molecule show the intramolecular features within the FePc and ZnPc molecules (figure 13(*d*) and (*f*)), in good agreement with the experimental results presented in figure 10(*d*) and 11(*d*), especially the asymmetry inside each lobe of the molecular orbital resolved images.

Finally, we want to point out that, during our experiments, after the tip-surface distance was reduced to pick up a molecule for functionalizing the tip, we did not find any MPc molecules missing from the MPc monolayer. Thus we can exclude the possibility of a MPc-functionalized STM tip. We have also systematically compared STM images simulated with the contaminants (of compositions Au, W, O, N, C, NO, CO, N_2, O_2) on different tips such as W-fcc(1 1 1), W-bcc(1 1 0) and Au-fcc(1 1 1). Among all of these calculated images, only the one calculated with an O_2 functionalized W(1 1 1) tip was in close agreement with experimental observation. Once this unique geometry and composition has been determined, we have verified by calculation that a rotation of 120° of the O_2 at the extremity of the apex does not introduce any significant modification in the simulated image. As this

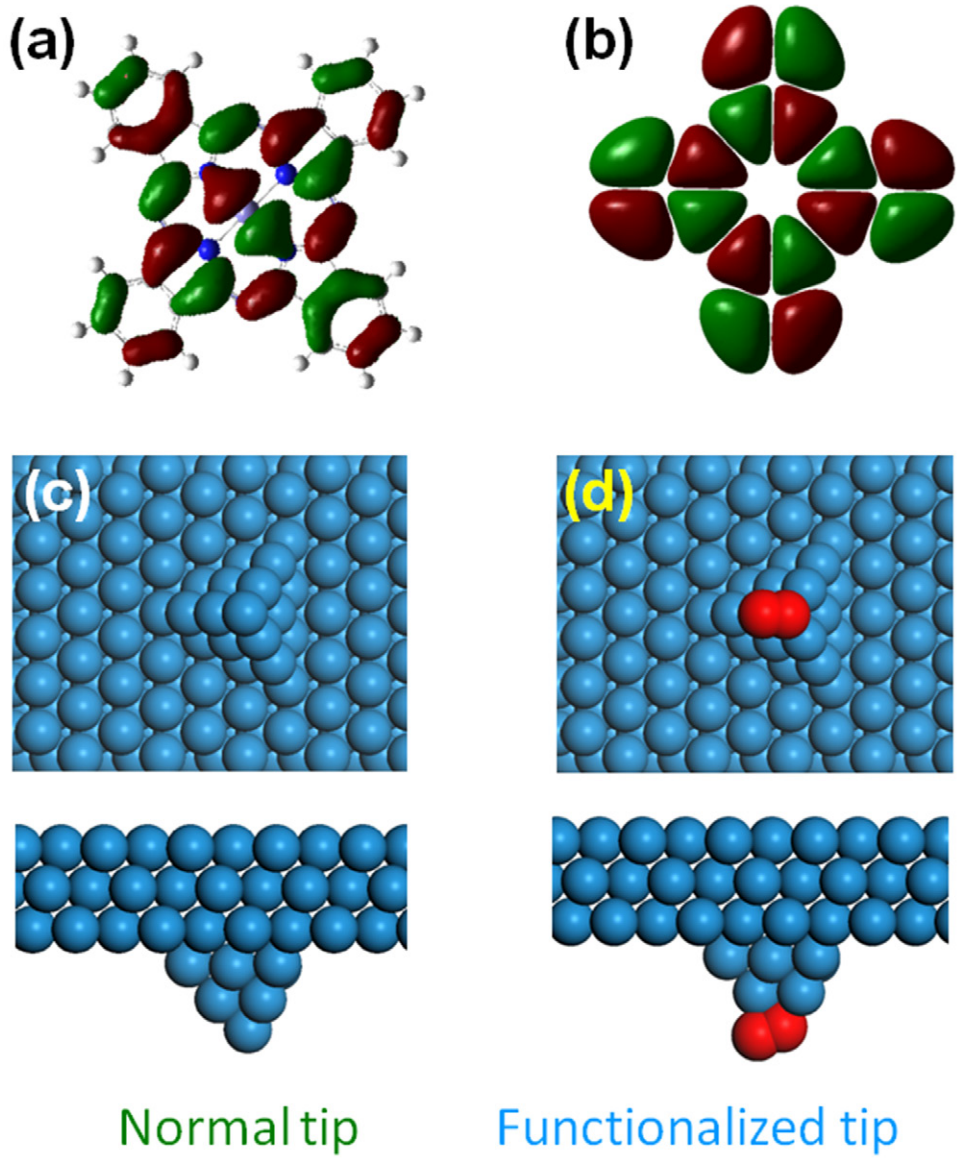

Figure 12. HOMOs of MPc (M = Fe or Zn) and STM tips used in simulation. (*a*) HOMO of FePc; (*b*) HOMO of ZnPc; (*c*) a sharp W(1 1 1) tip apex supported by a W slab: top view and side view; (*d*) O_2 functionalized blunt W(1 1 1) tip apex supported by a W slab: top view and side view (red balls are O atoms).

same functionalized tip was used directly to simulate STM images for ZnPc/Au(1 1 1) with excellent agreement, we may conclude that the special functionalized tip was indeed modified by oxygen molecules at the tip apex. Our results indicate that once well-controlled, the technique of functionalization of a tungsten tip with O_2 molecules could be a simple solution to improve the resolution of STM images of large molecules on metal surfaces.

4. Direct imaging of molecular intrinsic orbitals with a buffer layer

STM studies of individual molecules have usually been limited to molecules on metal or semiconductor substrates. In these cases, the electronic structure of the molecules is usually strongly influenced by the substrate either due to strong coupling between molecules and the substrate, or the fact that the molecular states are merged with the surface electrons to produce a convoluted STM image [14, 76]. Except for specific weakly adsorbed systems – for example, pentacene on Au(1 1 1 [16]) or anthracene on Ag(1 1 0 [17]) it is desirable to decouple molecules electronically from a substrate to investigate the intrinsic electronic properties of an individual molecule [77]. Ultra-thin insulating films (e.g. NaCl [12], oxides [78]) on a metallic substrate or passivated surface of a semiconductor have been used in the past to this end [20, 79]. Alternatively, organic thin films can form buffer layers to provide the decoupling [80–82]. In this section, we report two different kinds of buffer layer applied to observe the intrinsic electronic structure of molecules on metal substrates with STM [83, 84]. Each has distinctive advantages and can be

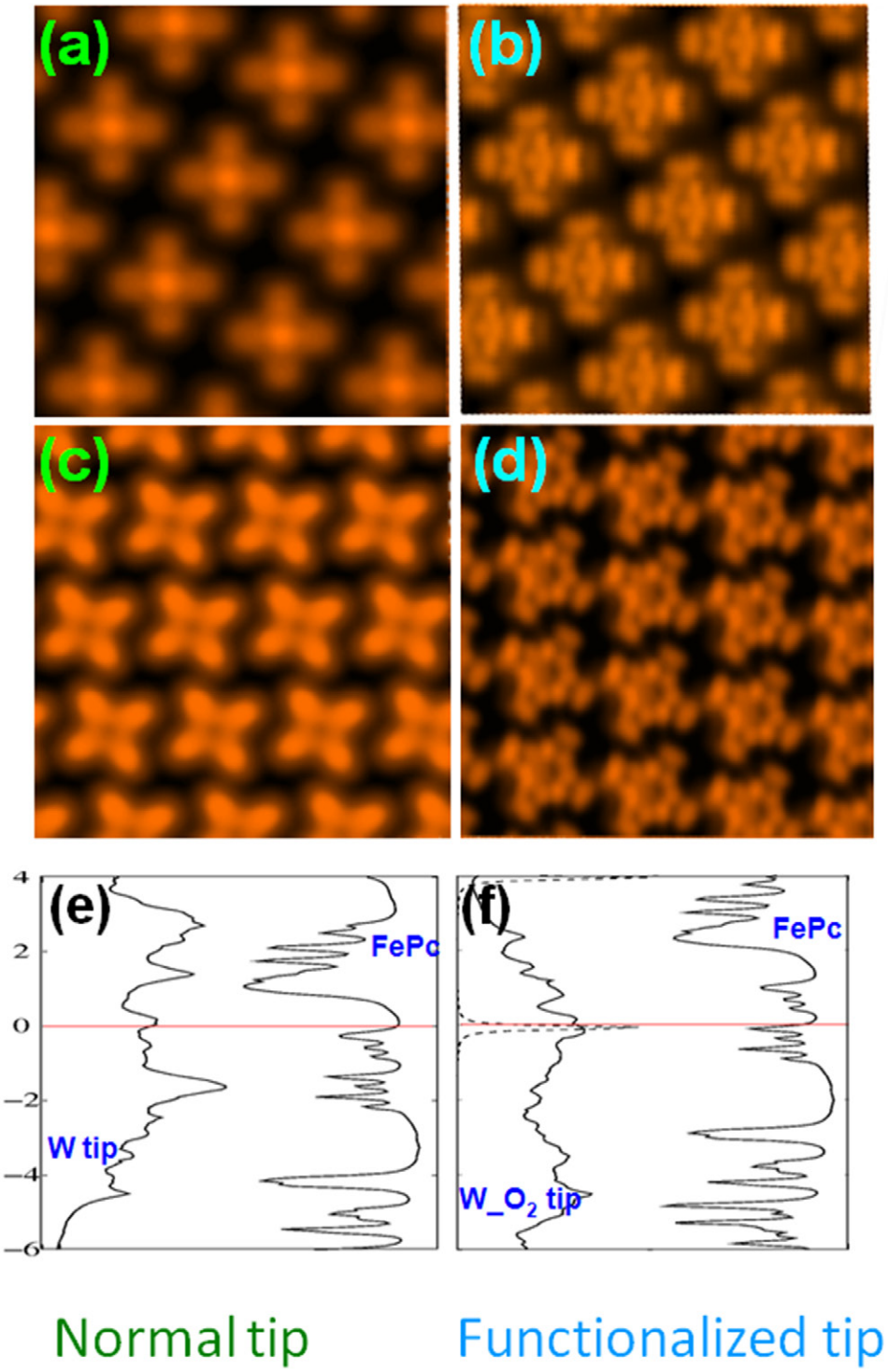

Figure 13. Simulated STM images and PDOS of tips/molecules. (*a*) FePc and (c) ZnPc on Au(1 1 1) with bare metallic STM tips; (*b*) FePc and (*d*) ZnPc on Au(1 1 1) with functionalized STM tips. (*e*) PDOS for FePc on Au(1 1 1) and the pure W(1 1 1) tip; (*f*) PDOS for FePc on Au(1 1 1) and the O_2 functionalized W(1 1 1) tip. The dashed lines are the DOS projected on O atoms. The horizontal lines indicate the Fermi level.

extended to a wide range of functional molecular systems for different applications.

4.1. The decoupling effect of an organic molecular layer

The intra-molecular features for individual orbitals of metal-phthalocyanine are difficult to resolved with a normal STM tip. Even when FePc is adsorbed on a thin decoupling layer of NaCl on Cu (1 1 1) the molecule is imaged as a cross without intrinsic features [13]. Here, we report on the direct observation of detailed electronic structures of the molecule using the decoupling effect of a molecular buffer layer. An FePc monolayer on a Au(1 1 1) substrate provides electronic decoupling to allow spatial variation of single electron states of individual

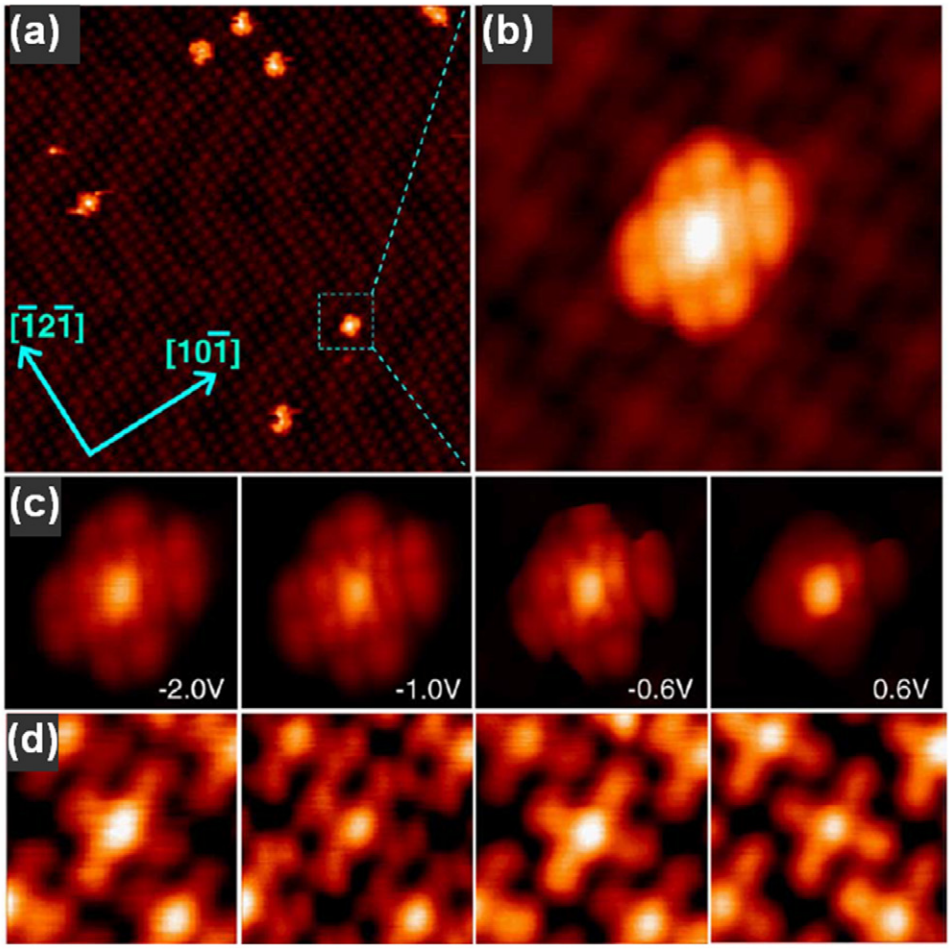

Figure 14. (*a*) Large-scale STM image of FePc molecules on highly ordered FePc monolayer on Au(1 1 1) (50 nm × 50 nm). (*b*) High-resolution STM image showing the adsorption site and configuration of an isolated FePc molecule on the monolayer (6 nm × 6 nm). $U = -2.0$ V, $I = 0.05$ nA, 77 K. (*c*) High-resolution STM images (3 nm × 3 nm, $I = 0.05$ nA) of the isolated FePc molecule adsorbed on the monolayer, taken at indicated sample biases. (*d*) The corresponding STM images (3 nm × 3 nm, $I = 0.05$ nA) of the FePc molecule directly adsorbed on Au(1 1 1).

FePc molecules to be studied. To verify that this is a generic effect, similar experimental observations were also conducted on (t-Bu)$_4$-ZnPc molecules at Au (1 1 1).

Experimentally, a highly-ordered FePc monolayer has been fabricated by evaporating FePc molecules onto the Au(1 1 1) surface [61, 83], showing a commensurate superstructure with a square unit cell. Figure 14(*a*) shows a constant-current STM image of an isolated FePc molecule adsorbed on the well-ordered FePc monolayer on Au(1 1 1). In figure 14(*b*) it is seen that features within this molecule appear distinctly only on the FePc buffer layer. High-resolution bias-dependent STM images are shown in figure 14(*c*) and (*d*). Figure 14(*c*) depicts an isolated FePc molecule adsorbed on the FePc monolayer, while figure 14(*d*) shows one FePc molecule within the buffer layer. The isolated FePc molecule on the monolayer exhibits spatially resolved internal structures at the indicated bias voltages; these internal structures are moreover bias-dependent. It should be noted that the internal structures at −2.0, −1.0 V and −0.6 V are very similar, while the images at −1.0 V are somewhat different. The internal structure at +0.6 V differs from those at negative bias voltages and is much less distinct. In the case of FePc molecules within the first monolayer adsorbed directly on Au(1 1 1), no spatially resolved inner structures are observed and nearly independent of the bias voltage, as shown in figure 14(*d*). This fact can be attributed to the influence of the metallic substrate. Due to the convolution of molecular states and electron states of the metal substrate, the inner structures cannot be clearly distinguished in the STM images with a tungsten tip. This result is in agreement with early STM simulations, which actually came to the conclusion that the spatial resolution of tungsten tips is rather poor [85].

This effect of an organic buffer layer on the resolution of the electronic structure can also be observed at other systems, such as (t-Bu)$_4$-ZnPc molecules. Isolated (t-Bu)$_4$-ZnPc molecules are dispersed and separate on an ordered (t-Bu)$_4$-ZnPc monolayer on Au(1 1 1), as shown in the large-scale STM image of figure 15(*a*). The (t-Bu)$_4$-ZnPc molecules of the monolayer are imaged as a four-lobed structure with a central hole. The four protrusions of one molecule show a rectangle, square or trapezoid due to the different substitution position of the tert-butyl groups on the benzene rings. Three (t-Bu)$_4$-ZnPc molecules with different shapes directly on Au(1 1 1)

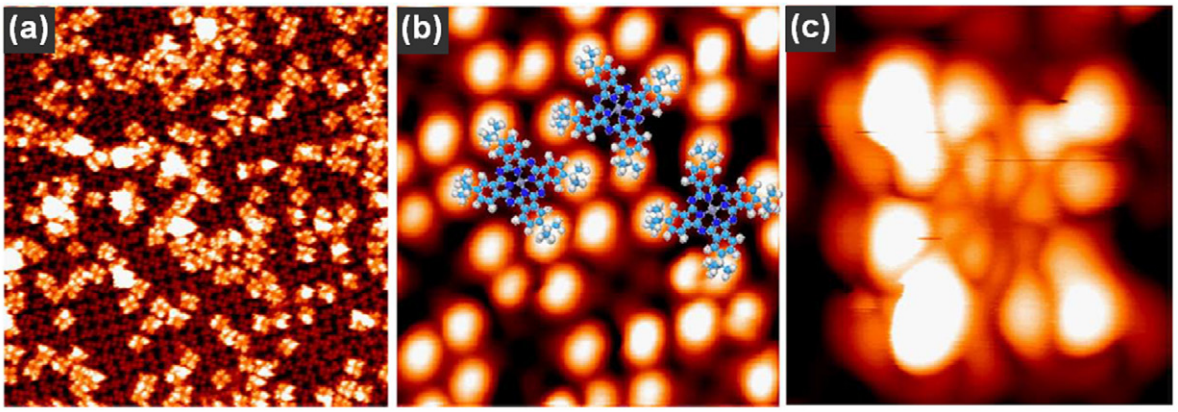

Figure 15. Isolated (t-Bu)$_4$-ZnPc molecules adsorbed on the ordered (t-Bu)$_4$-ZnPc monolayer on Au(1 1 1). (*a*) Large-scale STM image (50 nm × 50 nm, $U = -2.0$ V, $I = 0.05$ nA) of the distribution of (t-Bu)$_4$-ZnPc molecules on the monolayer. (*b*) Close-up STM image (5 nm × 5 nm, $U = -1.9$ V, $I = 0.03$ nA) of the ordered (t-Bu)$_4$-ZnPc monolayer on Au(1 1 1) surface. (*c*) Close-up STM image (4.5 nm × 4.5 nm, $U = -1.9$ V, $I = 0.03$ nA) showing the intramolecular features of the (t-Bu)$_4$-ZnPc molecule on the monolayer.

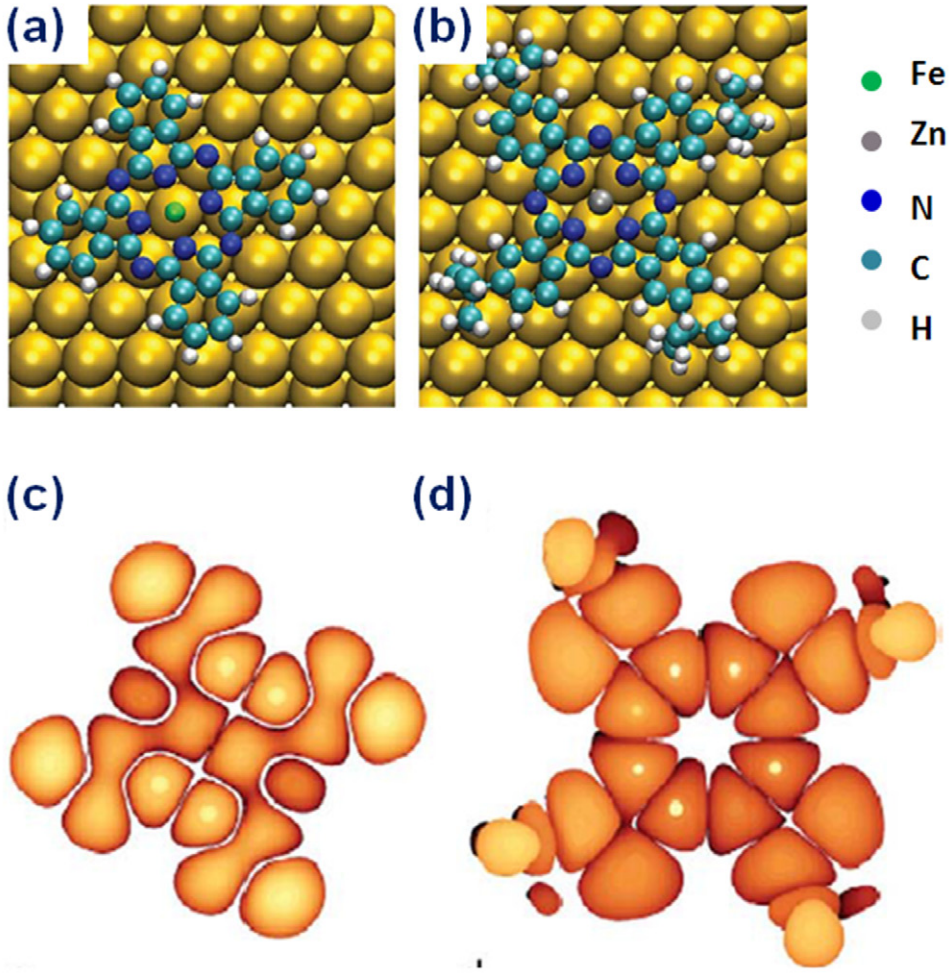

Figure 16. (*a*) and (*b*) The adsorption configurations of FePc and (tBu)$_4$-ZnPc molecules on Au(1 1 1), respectively. The metal center of the FePc molecule is adsorbed on top of an Au atom, while the metal center of the (tBu)$_4$-ZnPc molecule adsorbs at a bridge site. (*c*) The charge density contour of the highest occupied electronic state of FePc, and (*d*) shows the corresponding state for (tBu)$_4$-ZnPc.

are outlined in figure 15(*b*). This image structure indicates a flat-lying geometry. No spatially resolved inner structures can be observed within the molecules of the first monolayer on Au(1 1 1). The adsorption configurations of (t-Bu)$_4$-ZnPc molecules on the first monolayer are clearly shown in the STM image of figure 15(*c*). It represents a roughly flat-lying geometry with more detailed molecular features. This proves that the elimination of the background charge from the surface, which prevents imaging of detailed molecular states, is not a special feature of any particular molecule/substrate system.

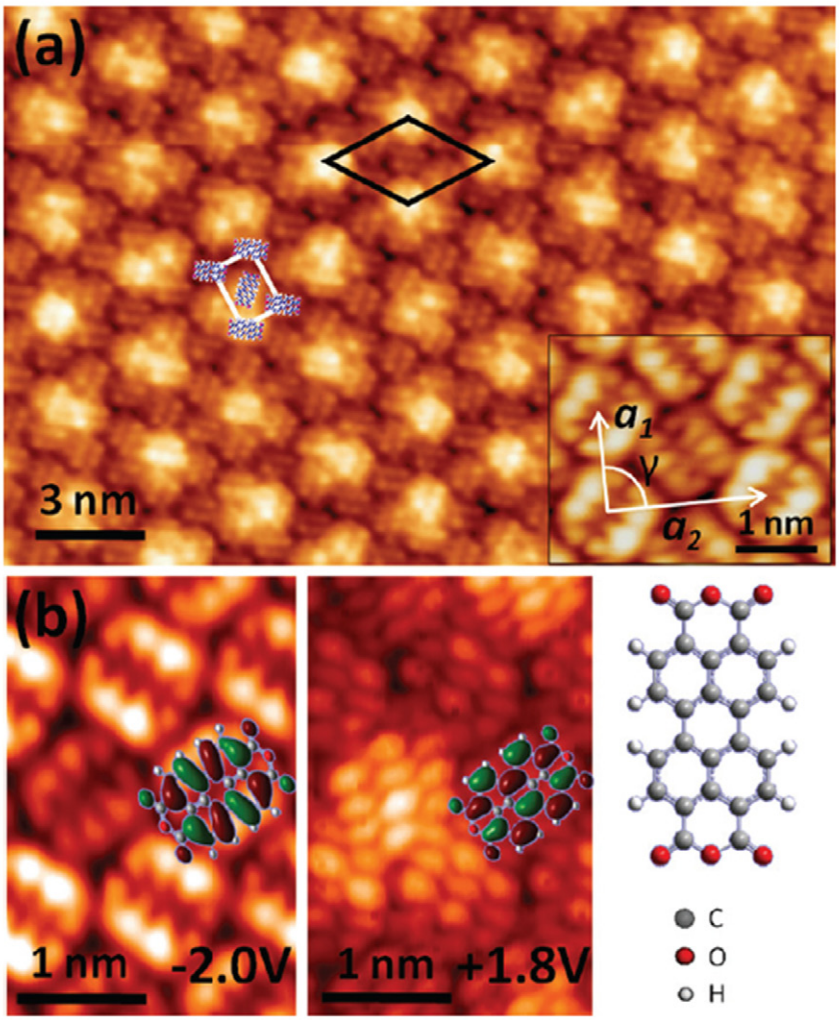

Figure 17. STM images of PTCDA molecules adsorbed on graphene/Ru(0 0 0 1). (*a*) Overview STM image, showing herringbone pattern. A rectangle and a rhombus are used to indicate the unit cells of the herringbone and moiré patterns, respectively. Inset displays a magnified unit cell with a_1 and a_2 denoting short and long lattice vectors. (*b*) High resolution images, showing HOMO (left panel) and LUMO (middle panel) with calculated orbitals superimposed. The right panel shows the molecular structure of PTCDA. Scanning parameters: (*a*) $U = -2.5$ V, $I = 0.05$ nA and (*b*) left: $U = -2.0$ V, $I = 0.10$ nA; middle: $U = 1.8$ V, $I = 0.20$ nA.

To determine the interaction between the molecules and the substrate, we constructed an Au(1 1 1) supercell model with four layers containing one FePc molecule. Figure 16(*a*) shows the adsorption site of FePc on Au(1 1 1). The optimized configuration shows that the distance between the molecule and the gold substrate is ~3.28 Å, indicating physisorption of the molecule, but no decisive changes of the molecular electronic structure due to hybridization of single electron states. The adsorption configuration of a $(tBu)_4$-ZnPc molecule on Au(1 1 1) is shown in figure 16(*b*). Both molecules are composed of a similar frame of nitrogen and carbon atoms; their key differences are the chemical identity of the metal center and the (t-Bu) groups attached to the benzene rings. These differences substantially change the appearance of the density contour of the highest occupied molecular state (HOMO).

For FePc, the density contour remains fairly flat with the ligands at approximately the same height as the molecular center (figure 16(*c*)). For $(tBu)_4$-ZnPc the highest protrusion of the contour is at the position of the (t-Bu) attachments, while the molecular center appears as a depression (figure 16(*d*)). These differences will have implications for the appearance of the molecule in actual STM experiments. A comparison with simulated STM image agrees well with the experimental data that the molecule directly on Au(1 1 1) is imaged as four distinct protrusions. Only in high resolution images of molecules on the buffer layer does the molecular appearance change to one close to the structure of HOMO. An isolated molecule on top of a molecular monolayer interacts only weakly via van der Waals forces, and will be situated at a distance above the surface, where the charge background from the surface has decayed enough to become effectively zero. In this case the electronic structure of the molecule is expected to be close to its state in the vacuum.

4.2. Epitaxially grown monolayer graphene on Ru(0 0 0 1)

Common buffer layers such as, organic molecules, NaCl and oxide thin films—used for passivating the substrates, face

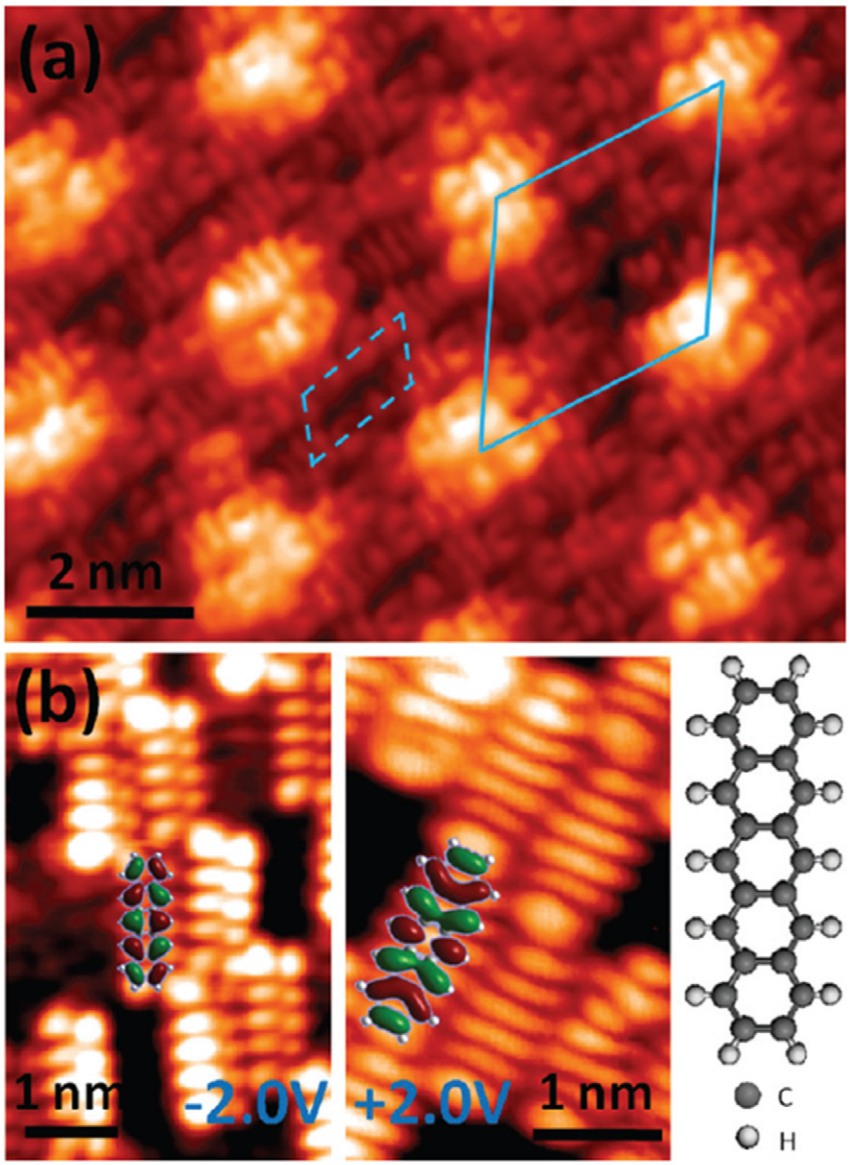

Figure 18. STM images of pentacene molecules adsorbed on graphene. (*a*) Overview image, showing compact side-by-side rows. A dashed parallelogram and a rhombus are overlaid to outline the unit cells of molecular film and moiré pattern, respectively. (*b*) High resolution images, showing HOMO (left panel) and LUMO (middle panel) with calculated orbitals superimposed. The right panel shows the molecular structure of pentacene. Scanning parameters: (*a*) $U = 2.0$ V, $I = 0.05$ nA and (*b*) left: $U = -2.0$ V, $I = 0.05$ nA; middle: $U = 2.0$ V, $I = 0.05$ nA.

several remaining issues. The surface of oxides is relatively inhomogeneous with small domain sizes and many defects [86], resulting in many different adsorption configurations of adsorbates [87]. In addition, buffer layers of organic films and NaCl cannot tolerate exposure to high temperatures and water, respectively. Recently, graphene monolayers epitaxially grown on various metal surfaces, for example, Ru(0 0 0 1) [88–90], Ir(1 1 1) [91], Pt(1 1 1) [92], Ni(1 1 1) [93], and Cu(1 1 1) [94] – have all attracted great interest due to their unique properties and potential applications for functional devices. Also, due to the increasing passions for graphene-based organic devices, much effort has also been expended on growing organic molecules on graphene [95, 96]. For instance, Barja *et al* investigated the self-organization of TCNQ and F4-TCNQ molecules on graphene, grown on Ir(1 1 1), and found the two molecules adopted distinct molecular orderings [95].

Next, we demonstrate that a large scale (centimeter), highly ordered, epitaxially grown graphene on Ru(0 0 0 1) can be used as a buffer layer for direct imaging of the intrinsic electronic structures of the adsorbed molecules. Combining STM experiments with DFT calculations, perylene-3,4,9,10-tetracarboxylic dianhydride(PTCDA), pentacene, and the fullerene (C_{60}) molecules are investigated. PTCDA, pentacene, and C_{60} molecules have been widely employed in understanding the mechanisms of molecular self-organization and in electronic devices such as organic photovoltaic cells [97, 98]. The graphene layer allows high resolution imaging of the detailed molecular orbitals of adsorbed molecules by decoupling the molecules electronically from the Ru(0 0 0 1) substrate.

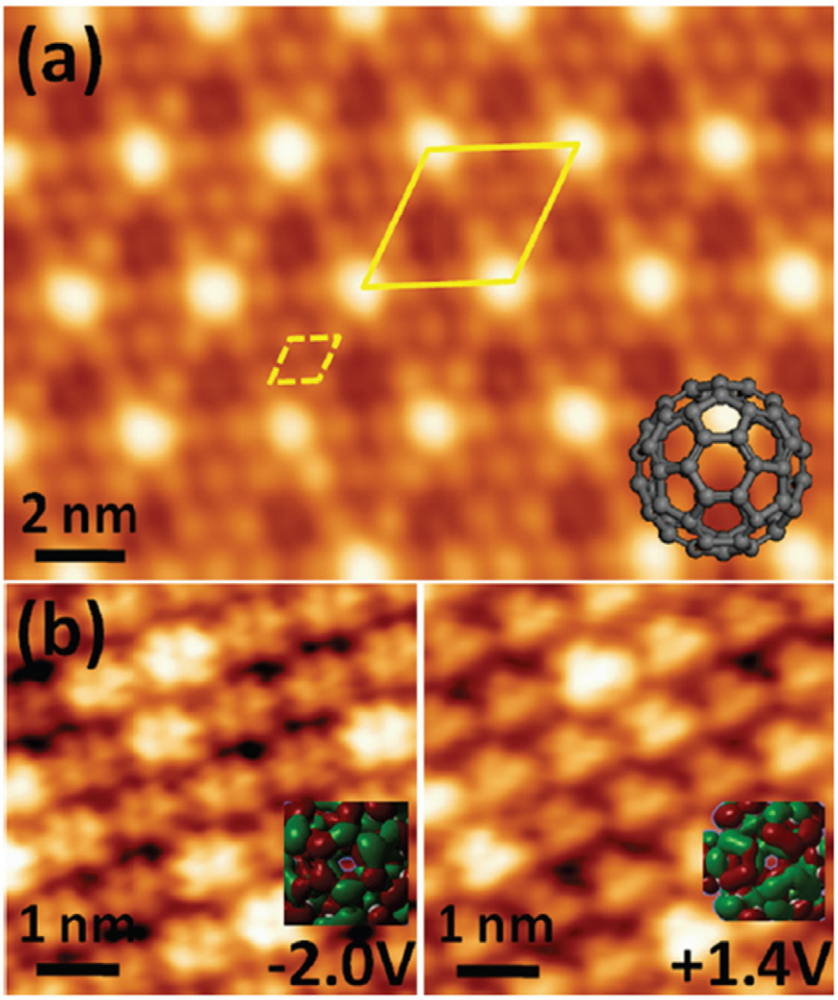

Figure 19. STM images of C60 molecules adsorbed on graphene. (*a*) Overview image, showing close-packed pattern. A dashed rhombus and a solid rhombus are overlaid to outline the unit cells of molecular film and moiré pattern, respectively. Inset shows the molecular structure with a hexagon facing up. (*b*) High resolution images, showing HOMO (left panel) and LUMO (right panel). The insets show the calculated results. Scanning parameters: (*a*) $U = 2.0$ V, $I = 0.05$ nA and (*b*) left: $U = -2.0$ V, $I = 0.10$ nA; right: $U = 1.4$ V, $I = 0.10$ nA.

The experiments were performed using a commercial Omicron LT-STM system. The Ru(0 0 0 1) surface was cleaned by cycles of argon-ion sputtering and annealing. High quality graphene was prepared by thermal decomposition of ethylene on this surface at high temperature. Single layer graphene on Ru(0 0 0 1) forms a regular moiré pattern, remaining continuous and defect-free, which is induced by a lattice mismatch between Ru(0 0 0 1) and graphene, with a periodicity of about 30 Å and an apparent corrugation of about 1 Å. Three regions can be clearly distinguished in this unit cell of the moiré superstructure, which are assigned to the top site, fcc site, and hcp site, respectively [88, 89].

PTCDA, pentacene, C_{60} (Sigma, 99 t%) molecules were thermally evaporated onto graphene at 620 K, 450 K, 600 K, respectively. During the evaporation process, the substrates were kept at 300 K for PTCDA and C60 and 330 K for pentacene. Subsequently, the samples were cooled down to 5 K for STM imaging.

PTCDA molecules are self-assembled into a herringbone pattern on the graphene/Ru(0 0 0 1), as shown in figure 17(*a*). A rectangle and molecular models are overlaid to indicate a unit cell of this pattern. In addition, another regular pattern appearing as six-fold symmetric bright spots can be clearly seen, whose unit cell is outlined by a rhombus. This pattern is due to the superimposition of underlying moiré superstructures on PTCDA films, and an analogous phenomenon has also been observed for molecular film on a reconstructed Au (1 1 1) surface, on which the reconstructed structure of a Au(1 1 1) substrate can be seen after molecular deposition [11]. The PTCDA molecules normally show a herringbone arrangement on various low index noble metal surfaces, such as Au (1 1 1) [99], Ag (1 1 1) [18, 99], and Cu (1 1 1) [100]. However, interactions between molecules and these surfaces, including bonding, image charges, and metal-mediated lateral interaction [101], give rise to a slight deformation of the herringbone unit cell compared to that of the (1 0 2) plane of PTCDA bulk structure [97]. In the inset of figure 17(*a*), we measure the lattice parameters of the unit cell for PTCDA on graphene/Ru(0 0 0 1), corresponding to $a_1 = 1.24$ nm, $a_2 = 1.93$ nm, and $\gamma = 90°$. Within the error limit, these three values are almost the same as those of a b-phase (1 0 2) plane of a PTCDA bulk structure, where $a_1 = 1.245$ nm, $a_2 = 1.930$ nm and $\gamma = 90°$ [97]. It indicates that

the interactions between PTCDA and graphene/Ru(0 0 0 1) are rather weak and inter-molecular interactions play a dominant role in the self-organization process.

The STM images of the HOMO and LUMO orbitals of PTCDA molecules are shown in figure 17(*b*), respectively. The bias voltage in our STM system is the voltage of the sample with respect to that of the tip, and thus negative and positive voltages correspond to HOMO and LUMO, respectively. These STM topographies fit very well with the calculated orbitals of a free molecule (as shown in the insets of figure 17(*b*)), which further verifies that the substrate exerts a weak influence and the intrinsic molecular orbitals are well preserved. Here the STM image of LUMO orbitals of PTCDA is consistent with the earlier results of PTCDA submolecular structure on Ag(1 1 1) and Ag (1 1 0), in which six inner lobes and four outer lobes are resolved [18, 23]. Although there is covalent bonding of PTCDA to the Ag surfaces, the contribution of Ag states to the unoccupied LDOS near Fermi level is very limited, so that it looks similar on physisorption surfaces like HOPG [102] or MoS_2 [103].

Pentacene and C_{60} molecules formed compact rows side by side and close-packed patterns, respectively, as shown in figures 18(*a*) and 19(*a*). Similar to the case of PTCDA, the unit cells of both molecular films and moiré patterns are outlined in the images. For pentacene, as presented in figure 18(*b*), the topographies agree well with the calculated results as shown in the insets. For C_{60}, the HOMO and LUMO images are in doughnut and three-leaf shapes, respectively (see figure 19(*b*)). Previous calculations suggest that the HOMO state is spatially located on C=C (double) bonds and the LUMO state on C–C (single) bonds [104, 105]. Also, it is known that every bond shared by two adjacent hexagonal rings is an essential double bond, while that on pentagonal rings is a single bond in C_{60}. When we probe a C_{60} molecule with a hexagonal ring facing up (as shown in the inset of figure 19(*a*)), at negative bias (corresponding to HOMO), the double-bonded hexagonal rings are mainly detected, showing a doughnut image (left panel of figure 19(*b*)). While at positive bias (corresponding to LUMO), the single bonded pentagonal rings are mainly detected, showing a three-leaf image (right panel of figure 19(*b*)). The topography images and above analysis agree well with the theoretical and experimental results of C_{60} from other groups [104–107]. Thereby, based on these high resolution images, we can safely conclude that all the C_{60} molecules in the images adopt the same adsorption configuration with a hexagonal ring at the topmost position.

5. Conclusions

We have reviewed the high resolution STM imaging of Si(1 1 1)-7×7 reconstruction structure and adsorbed functional molecules on substrates. For the Si(1 1 1)-7×7 surface, classical STM images reveal only the 12 adatom spots to a large extent of the bias applied. We show, for the first time, clearly resolved STM images of the six rest atoms and the 12 adatoms on the Si(1 1 1)-7×7 unit cell simultaneously. These results are in good agreement with those obtained by first-principles calculations. It demonstrates that the STM can probe the real-space charge distribution far below the Fermi level at corresponding bias voltage if a geometric hindrance, due to the finite size of the tip apex, can be removed.

STM has been demonstrated to be powerful for probing directly the intrinsic electronic structure of individual molecules on solid surfaces. Various strategies, including functionalizing a STM tip and adding a buffer layer on metal substrates, have been developed. The selective imaging of molecular states of perylene adsorbed on Ag(1 1 0) is achieved by functionalizing the STM tip with a perylene molecule, which leads to a mismatch between the energy levels of the tip and the molecule adsorbates and images only the metal states of the underlying silver surface. In another example, rich intramolecular features of metal-Pc molecules on Au(1 1 1) were revealed by using a special O_2 decorated tip due to the interaction with the highly directional orbitals of the adsorbed O_2 molecules.

For the applications of buffer layers, we present a proof that an organic molecular layer on a metal substrate provides sufficient decoupling from the metal charge background to allow the inherent electronic properties of individual molecules to become visible in STM. Epitaxially grown single-layer graphene on Ru(0 0 0 1) can also work as a powerful buffer layer to disentangle the molecular electronic structure from the influence of Ru(0 0 0 1) substrate, and then allows the direct imaging of the electronic orbitals of the adsorbed molecules. Importantly, it is in a large scale (centimeter in size), almost defect-free, tolerant of high temperature (~1300 K) and water. Thus, it has a promising application in fundamental research based on electronic state studying of molecules on metals, with similar chemical reactions and catalysis mechanisms.

Acknowledgements

We are grateful to H W Liu, D X Shi, L Gao, Z T Deng, Z H Cheng, N Jiang, H T Zhou, and J H Mao for experimental assistance, and I G Batyrev, W E McMahon, S B Zhang, H Lin, Y Y Zhang, H Tang, and W A Hofer for theory simulations and calculations. This research is supported by the Natural Science Foundation of China and the Chinese National '863' and '973' projects.

References

[1] Binnig G, Rohrer H, Gerber C and Weibel E 1982 *Phys. Rev. Lett.* **49** 57
[2] Eigler D M and Schweizer E K 1990 *Nature* **344** 524
[3] Lyo I W and Avouris P 1991 *Science* **253** 173
[4] Uchida H, Huang D H, Grey F and Aono M 1993 *Phys. Rev. Lett.* **70** 2040
[5] Salling C T and Lagally M G 1994 *Science* **265** 502
[6] Khan Y, Al-Falih H, Zhang Y P, Ng T K and Ooia B S 2012 *Rev. Sci. Instrum.* **83** 063708
[7] Nonnenmacher M, O'Boyle M P and Wickramasinghe H K 1991 *Appl. Phys. Lett.* **58** 2921
[8] Borzenets I V, Yoon I, Prior M W, Donald B R, Mooney R D and Finkelstein G 2012 *J. Appl. Phys.* **111** 074703
[9] Liu L W *et al* 2013 *Sci. Rep.* **3** 1210

[10] Foster A S and Hofer W A 2006 *Scanning Probe Microscopy: Atomic Scale Engineering by Forces and Currents* (New York: Springer)
[11] Gao H J and Gao L 2010 *Prog. Surf. Sci.* **85** 28
[12] Repp J, Meyer G, Stojković S M, Gourdon A and Joachim C 2005 *Phys. Rev. Lett.* **94** 026803.
[13] Scarfato A, Chang S H, Kuck S, Brede J, Hoffmann G and Wiesendanger R 2008 *Surf. Sci.* **602** 677
[14] Wang Y, Krögeer J, Berndt R and Hofer W 2009 *Angew. Chem. Int. Ed.* **48** 1261
[15] Ge X, Manzano C, Berndt G, Anger L T, Köhler F and Herges R 2009 *J. Am. Chem. Soc.* **131** 6096
[16] Soe W H, Manzano C, De Sarkar A, Chandrasekhar N and Joachim C 2009 *Phys. Rev. Lett.* **102** 176102
[17] Boehringer M, Schneider W D and Berndt R 1998 *Surf. Sci.* **408** 72
[18] Gloeckler K, Seidel C, Soukopp A, Sokolowski M, Umbach E, Boehringer M, Berndt R and Schneider W D 1998 *Surf. Sci.* **405** 1
[19] Boehringer M, Schneider W D, Gloeckler K, Umbach E and Berndt R 1998 *Surf. Sci.* **419** L95
[20] Bellec A, Ample F, Riedel D, Dujardin G and Joachim C 2009 *Nano Lett.* **9** 144
[21] Eigler D M, Lutz C P and Rudge W E 1991 *Nature* **352** 600
[22] Bartels L, Meyer G and Rieder K H 1997 *Appl. Phys. Lett.* **71** 213
[23] Boehringer M and Schneider W D 1998 *Phys. Rev.* B **57** 4081
[24] Bartels L, Meyer G and Rieder K H 1999 *Surf. Sci.* **432** L621
[25] Haln J R and Ho W 2001 *Phys. Rev. Lett.* **87** 196102
[26] Hagelaar J H A, Flipse C F and Cerda J L 2008 *Phys. Rev.* B **78** 161405
[27] Sugimoto Y, Pou P, Abe M, Jelinek P, Perez R, Morita S and Custance O 2007 *Nature* **446** 64
[28] Gross L, Mohn F, Moll N, Liljeroth P and Meyer G 2009 *Science* **325** 1110
[29] Zhang J, Chen P C, Yuan B K, Ji W, Cheng Z H and Qiu X H 2013 *Science* **342** 611
[30] Binnig G, Rohrer H, Gerber C and Weibel E 1983 *Phys. Rev. Lett.* **50** 120
[31] Takayanagi K, Tanishiro Y, Takahashi M and Takahashi S 1985 *J. Vac. Sci. Technol.* **3** 1502
[32] Avouris P and Wolkow R 1989 *Phys. Rev.* B **39** 5091
[33] Nishikawa O, Tomitori M, Iwawaki F and Hirano N 1990 *J. Vac. Sci. Technol. A* **8** 421
[34] Lantz M A, Hug H J, Schendel P, Hoffmann R, Martin S, Baratoff A, Abdurixit A, Güntherodt H J and Gerber C 2000 *Phys. Rev. Lett.* **84** 2642
[35] Giessibl F J, Hembacher S, Bielefeldt H and Mannhart J 2000 *Science* **289** 422
[36] Giessibl F J 1995 *Science* **267** 68
[37] Sutter P, Zahl P, Sutter E and Bernard L E 2003 *Phys. Rev. Lett.* **90** 166101
[38] Hamers R J, Tromp R M and Demuth J E 1986 *Phys. Rev. Lett.* **56** 1972
[39] Becker R S, Swartzentruber B S, Vickers J S and Klitsner T 1989 *Phys. Rev.* B **39** 1633
[40] Chen L, Pan B C, Xiang H J, Wang B, Yang J L, Hou J G and Zhu Q S 2007 *Phys. Rev.* B **75** 085329
[41] Wiesendanger R 1994 *Scanning Probe Microscopy and Spectroscopy: Methods and Applications* (Cambridge: Cambridge University Press)
[42] Zhang S B, Cohen M L and Louie S G 1986 *Phys. Rev.* B **34** 768
[43] Kresse G and Furthmüller J 1996 *Comput. Mater. Sci.* **6** 15
[44] Vanderbilt D 1990 *Phys. Rev.* B **41** 7892
[45] Tersoff J and Hamann D R 1985 *Phys. Rev.* B **31** 805
[46] Wang Y L, Gao H J, Guo H M, Liu H W, Batyrev I G, McMahon W E and Zhang S B 2004 *Phys. Rev.* B **70** 073312
[47] Lemay S G *et al* 2001 *Nature* **412** 617
[48] Nazin G V, Qiu X H and Ho W 2003 *Science* **302** 77
[49] Joachim C, Gimzewski J K and Aviram A 2000 *Nature* **408** 541
[50] Emberly E G and Kirczenow G 2003 *Phys. Rev. Lett.* **91** 188301
[51] Kuntze J, Berndt R, Jiang P, Tang H, Gourdon A and Joachim C 2002 *Phys. Rev.* B **65** 233405
[52] Rubinson J F and Mark H B 2002 *Conductive Polymers and Polymer Electrolytes: From Biology to Photovoltaics* (Washington, DC: American Chemical Society)
[53] Skotheim T A, Elsenbaumer R L and Reynolds J R 1998 *Handbook of Conducting Polymers* 2nd ed (New York: Dekker)
[54] Seidel C, Ellerbrake R, Gross L and Fuchs H 2001 *Phys. Rev.* B **64** 195418
[55] Kresse G and Furthmunller J 1996 *Phys. Rev.* B **54** 11169
[56] Kresse G and Hafner J 1993 *Phys. Rev.* B **47** 558
[57] Perdew J P, Chevary J A, Vosko S H, Jackson K A, Pederson M R, Singh D J and Fiolhais C 1992 *Phys. Rev.* B **46** 6671
[58] Palotas K and Hofer W A 2005 *J. Phys.: Condens. Matter* **17** 2705
[59] Deng Z T *et al* 2006 *Phys. Rev. Lett.* **96** 156102
[60] Mittendorfer F and Hafner J 2001 *Surf. Sci.* **472** 133
[61] Cheng Z H *et al* 2007 *J. Phys. Chem. C* **111** 2656
[62] Cheng Z H *et al* 2011 *Nano Res.* **4** 523
[63] Lu X and Hipps K W 1997 *J. Phys. Chem.* B **101** 5391
[64] Yoshimoto S, Tsutsumi E, Suto K, Honda Y and Itaya K 2005 *Chem. Phys.* **319** 147
[65] Liao M S and Scheiner S 2001 *J. Chem. Phys.* **114** 9780
[66] Bohrer F I, Sharoni A, Colesniuc C, Park J, Schuller I K, Kummel A C and Trogler W C 2007 *J. Am. Chem. Soc.* **129** 5640
[67] Sabelli N H and Melendres C A 1982 *J. Phys. Chem.* **86** 4342
[68] Zhivkov I 2009 *J. Optoelectron. Adv. Mater.* **11** 1396
[69] Dahlberg S C and Musser M E 1980 *J. Chem. Phys.* **72** 6706
[70] Perdew J P, Burke K and Wang Y 1996 *Phys. Rev.* B **54** 16533
[71] Blöchl E 1994 *Phys. Rev.* B **50** 17953
[72] Cerdá J, Van Hove M A, Sautet P and Salmeron M 1997 *Phys. Rev.* B **56** 15885
[73] Cerdá J, Yoon A, Van Hove M A, Sautet P, Salmeron M and Somorjai G A 1997 *Phys. Rev.* B **56** 15900
[74] Cerdá J and Soria F 2000 *Phys. Rev.* B **61** 7965
[75] Lucier A S, Mortensen H and Grütter P 2005 *Phys. Rev.* B **72** 235420
[76] Gao L *et al* 2007 *Phys. Rev. Lett.* **99** 106402
[77] Langlais V J, Schlittler R R, Tang H, Gourdon A, Joachim C and Gimzewski J K 1999 *Phys. Rev. Lett.* **83** 2809
[78] Qiu X H, Nazin G V and Ho W 2003 *Science* **299** 542
[79] Villagomez C J, Zambelli T, Gauthier S, Gourdon A, Stojkovic S and Joachim C 2009 *Surf. Sci.* **603** 1526
[80] Feng M *et al* 2007 *Adv. Func. Mater.* **17** 770
[81] Cuberes M T, Schlittler R R and Gimzewski J K 1998 *Appl. Phys.* A **66** S745
[82] Guo X L, Dong Z C, Trifonov A S, Yokoyama S, Mashiko S and Okamoto T 2004 *Appl. Phys. Lett.* **84** 969
[83] Cheng Z H, Du S X, Jiang N, Zhang Y Y, Guo W, Hofer W A and Gao H J 2011 *Surf. Sci.* **605** 415
[84] Zhou H T, Mao J H, Li G, Wang Y L, Feng X L, Du S X, Muellen K and Gao H J 2011 *Appl. Phys. Lett.* **99** 153101
[85] Hofer W A and Redinger J 2000 *Surf. Sci.* **447** 51
[86] Stierle A, Renner F, Streitel R, Dosch H, Drube W and Cowie B C 2004 *Science* **303** 1652
[87] Wu S W, Ogawa N and Ho W 2006 *Science* **312** 1362
[88] Pan Y, Zhang H G, Shi D X, Sun J T, Du S X, Liu F and Gao H J 2009 *Adv. Mater.* **21** 2777
[89] Pan Y, Shi D X and Gao H J 2007 *Chin. Phys.* **16** 3151
[90] Mao J H *et al* 2012 *Appl. Phys. Lett.* **100** 093101

[91] N'Diaye A T, Bleikamp S, Feibelman P J and Michely T 2006 *Phys. Rev. Lett.* **97** 215501
[92] Gao M, Pan Y, Huang L, Hu H, Zhang L Z, Guo H M, Du S X and Gao H J 2011 *Appl. Phys. Lett.* **98** 033101
[93] Dedkov Y S, Fonin M, Rudiger U and Laubschat C 2008 *Phys. Rev. Lett.* **100** 107602
[94] Li X S *et al* 2009 *Science* **324** 1312
[95] Barja S, Garnica M, Hinarejos J J, De Parga A L V, Martin N and Miranda R 2010 *Chem. Commun.* **46** 8198
[96] Wang Q H and Hersam M C 2009 *Nat. Chem.* **1** 206
[97] Tautz F S 2007 *Prog. Surf. Sci.* **82** 479
[98] Peumans P and Forrest S R 2001 *Appl. Phys. Lett.* **79** 126
[100] Wagner T, Bannani A, Bobisch C, Karacuban H and Moller R 2007 *J. Phys.: Condens. Matter* **19** 056009
[101] Hauschild A, Karki K, Cowie B C C, Rohlfing M, Tautz F S and Sokolowski M 2005 *Phys. Rev. Lett.* **94** 036106
[102] Hoshino A, Isoda S, Kurata H and Kobayashi T 1994 *J. Appl. Phys.* **76** 4113
[103] Ludwig C, Gompf B, Petersen J, Strohmaier R and Eisenmenger W 1994 *Z. Phys.* B **93** 365
[104] Wang L L and Cheng H P 2004 *Phys. Rev. B* **69** 165417
[105] Maruyama Y, Ohno K and Kawazoe Y 1995 *Phys. Rev.* B **52** 2070
[106] Lu X H, Grobis M, Khoo K H, Louie S G and Crommie M F 2004 *Phys. Rev.* B **70** 115418
[107] Rossel F, Pivetta M, Patthey F, Cavar E, Seitsonen A P and Schneider W D 2011 *Phys. Rev.* B **84** 075426